A Laplace-Domain Hybrid Model for Representing Flow Behavior of Multifractured Horizontal Wells Communicating Through Secondary Fractures in Unconventional Reservoirs

Pin Jia and **Linsong Cheng,** China University of Petroleum, Beijing; **Christopher R. Clarkson** and **Farhad Qanbari,** University of Calgary; and **Shijun Huang** and **Renyi Cao,** China University of Petroleum, Beijing

Summary

In a multiwell pad, the chance of interwell communication increases because of the creation of primary and secondary fractures during hydraulic-fracture stimulation. The flow behavior associated with communicating wells is significantly different from that of a single isolated well, because of interplay of flow caused by the interconnected fractures, complex connections, and multiple production conditions. The main purpose of this paper is to develop a rigorous and efficient flow model and quantify flow characteristics of multiple pad wells communicating through primary and secondary fractures.

In the model, matrix and primary- and secondary-fracture flows are captured. Fractures are explicitly represented by discrete segments. The Laplace-transform finite-difference (LTFD) method is used to numerically model fracture flow, with sufficient flexibility to consider arbitrary fracture geometries and fracture-conductivity distributions. The analytical matrix-flow model, derived with the line-source function in the Laplace domain, is dynamically coupled with the fracture-flow model, by imposing the continuity of pressure and flux on the fracture surface. Thus, a hybrid model in the Laplace domain is constructed. The main advantage of the solution occurring in Laplace domain is that computations can be performed at predetermined, discrete times, and with grids only for fractures. Thus, stability and convergence problems caused by time discretization are avoided, and the burden of gridding and computation is decreased without loss of important fracture characteristics.

The model is validated through comparison with a fully numerical simulator and a semi-analytical model. Detailed flow-regime analysis reveals that pressure interference caused by communication significantly alters the flow signature compared with single (isolated) wells. Before interference, the communicating wells behave as single isolated wells, and will exhibit a fracture linear-flow period and possibly even a matrix linear-flow period. After interference, the flow behavior of the system will vary largely with different production strategies. When the communicating wells all operate under the constant-rate condition, the transient responses of the wells will gradually merge to develop another matrix linear-flow period. If the wells are operated under the constant-bottomhole-pressure (BHP) conditions, the response deviation caused by interference will increase with production; therefore, one of the wells will undergo a rate loss. The results of a sensitivity analysis for a two-well system demonstrate that the time to well interference is primarily determined by secondary-fracture conductivity, number of connections, and communicating-well operating conditions. With larger contrasts in these properties, interference time is accelerated. However, for different production strategies, the effects on the flow behavior after interference are variable.

Introduction

In recent years, with the downturn in oil prices, improvement in hydraulic-fracturing-stage design and well-location optimization has received widespread attention in unconventional reservoirs. One of the most common field developments is infill drilling into drill-to-hold leases. With high well density, the chance of multiwell communication will increase because of the occurrence of complex fracture connections, also known as "fracture hits" (Lawal et al. 2013; Yaich et al. 2014; Marongiu-Porcu et al. 2016), as illustrated in **Fig. 1.** The "fracture hits" are also apparently indicated by the observation of field data (wellbore-pressure perturbation or production-rate drop for no apparent reason). As shown in **Fig. 2,** a rate decrease in the producing well (shown in black) occurs at Day 72, which corresponds to the same time an offset well (shown in red) was hydraulically stimulated. As a result, the producing well (shown in black) exhibits a rate loss of approximately 1,300 Mscf/D. This rapid change in production rate is believed to be the direct result of flow between communicating fractures (Lawal et al. 2013). In this situation, primary hydraulic fractures of each well (between at least two wells) will possibly be connected by secondary fractures (e.g., activated pre-existing natural fractures). This phenomenon in a multiwell pad has increased the complexity of well and stage location optimization. Therefore, modeling the flow behavior of multiwell communication is important for evaluating the effects of multiwell interference and how well performance is affected.

Currently, the most common approach to simulate the production of multiple wells is full numerical simulation. Well performance of multiple wells communicating through interconnected fractures has been extensively investigated by use of commercial reservoir numerical-simulation software (Gupta et al. 2012; Martinez et al. 2012; Lawal et al. 2013; Yaich et al. 2014; Malpani et al. 2015). Also, transient-pressure analysis of a multiwell pad has been used to identify well communication (Portis et al. 2013; Sardinha et al. 2014; Sani et al. 2015). In the previous studies with these techniques, the authors used single or multiple transverse fractures to perform predictions of multifractured-horizontal-well performance, caused by the difficulties in modeling arbitrary fracture geometries in commercial software. Historical studies have often approximated complex hydraulic-fracture networks as planar, symmetric biwing fractures and lose some details of fracture characteristics. Recently, Marongiu-Porcu et al. (2016) investigated interwell-fracture interference by use of a state-of-the-art modeling work flow. A multidisciplinary approach is successfully implemented to capture formation properties,

Original SPE manuscript received for review 6 January 2017. Revised manuscript received for review 20 April 2017. Paper (SPE 186109) peer approved 25 April 2017.

hydraulic-fracture propagation, and interactions with pre-existing natural fractures. Production simulation with the work flow essentially follows the idea of an unconventional fracture model (UFM) developed by Cipolla et al. (2011), which integrates an extensive adaptive gridding scheme and numerical simulation to forecast the performance of complex-fracture networks. Nevertheless, because of the complexity of the UFM and associated grid discretization, the approach may involve a more difficult model setup and increased computation time caused by a large number of cells and small timesteps required to obtain sufficiently accurate results.

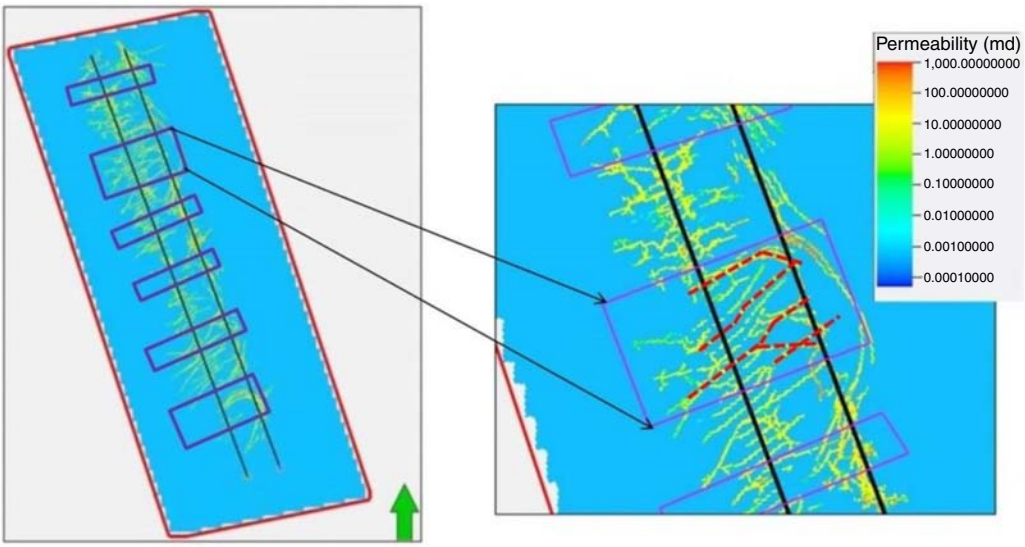

Fig. 1—Illustration of interwell communication. (Left) Fracture geometry of a parent well and a child well (infill well); purple rectangles depict the fracture-interconnecting region. (Right) Magnified view of the largest fracture-interconnecting region to better illustrate the fracture geometry. Dashed red lines are used to indicate some interconnected fractures (modified from Marongiu-Porcu et al. 2016).

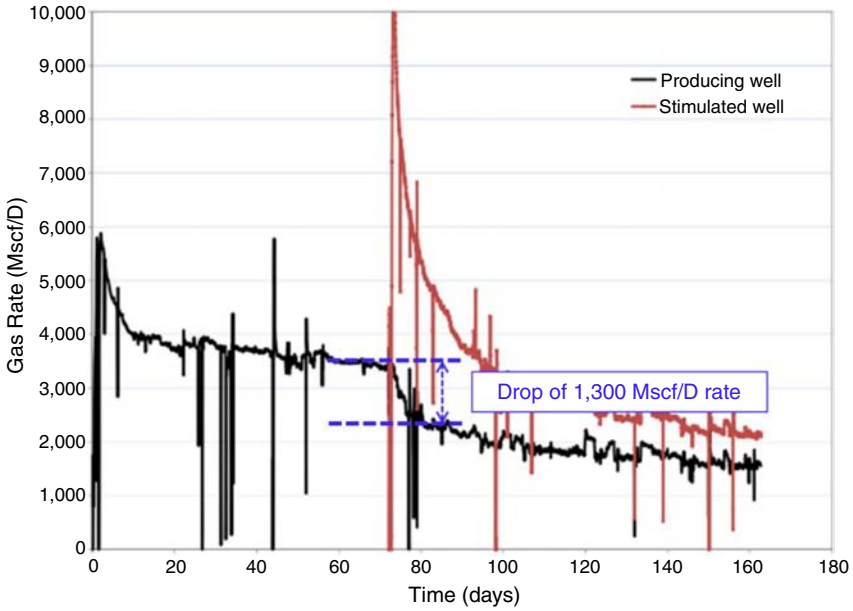

Fig. 2—Production-rate profile of one existing producing well and one stimulated well for indication of well communication through secondary fractures (modified from Lawal et al. 2013).

By use of Green's function provided by Gringarten and Ramey (1973), Awada et al. (2016) adopted a simple analytical solution to investigate multiwell communication with connected fractures from two adjacent wells. The model assumed biwing uniform-conductivity vertical fractures within a closed rectangular reservoir (Earlougher and Ramey 1973). Awada et al. (2016) concluded that fracture conductivity significantly influences the timing and pressure response of interference. However, the analytical model was restrictive, assuming a single planar fracture for each well with uniform- or infinite-conductivity fractures. Hence, their approach is difficult to extend to the simulation of production for the case of multiple fractures with varying fracture conductivity connected by complex fractures (e.g., some secondary fractures with different inclinations).

Yu et al. (2016) built a comprehensive semianalytical model to quantitatively simulate the rate response of multiwell interference with fracture hits. The model essentially used a node-analysis approach to discretize the complex-fracture network into grids for numerical simulation, and adopted Green's function in the real domain to derive an analytical reservoir flow solution. The multiwell case was simulated with constant BHP constraint. The study provided and improved understanding of the performance of well-interference

through fracture hits. The disadvantage of solutions on the basis of Green's function in the real domain is that the simulation results are still dependent on timesteps, and the speed of computation will decrease with simulation time, because of the need for pressure superposition of previous timesteps. Further, the assumption of steady-state flow within fractures in the model may affect the accuracy of time and pressure responses caused by interference. Awada et al. (2016) pointed out that interference responses will occur within the first 10 minutes for a fracture permeability greater than $1{,}000 \times 10^{-3}\mu m^2$. In addition, although significant efforts have been made to develop efficient models for simulation of complex-fracture networks (Hazlett and Babu 2014; Zhou et al. 2014; Jia et al. 2015), most studies only focus on single wells, and the effects of multiwell interference are not accounted for or discussed.

Therefore, there is still a need to develop a more-efficient and -rigorous approach to model the transient-flow behavior of multiwell communication through interconnected fractures and to investigate the flow signatures of communicating wells. In this paper, we therefore develop a Laplace-domain hybrid model to simulate production from such a system more efficiently and rigorously. In the model, flow from the matrix to the wellbore is assumed to occur by means of fracture flow and matrix flow. We use the LTFD method to numerically model fracture flow in discrete fracture segments. The analytical matrix-flow model, derived with the line-source function in the Laplace domain, is dynamically coupled with the fracture-flow model by use of production boundary conditions. The main advantage of the hybrid solution in the Laplace domain is that computations can be performed at predetermined, discrete times, and with grids only for fractures. The use of discrete fracture segments provides sufficient flexibility to consider complex fracture geometries and varying conductivities. Thus, stability and convergence problems caused by time discretization are avoided, and the burden of gridding and computation is decreased without loss of important fracture characteristics. In addition, unsteady-state flow in fractures is considered, and each well can operate with different production constraints: constant rate or constant BHP. By use of the new model, type curves are plotted, and flow behavior is analyzed in detail. The effects of secondary-fracture conductivity, number of fracture connections, and operating conditions are also discussed.

Importantly, the new model developed in this work can be used to diagnose well communication though history-matching and forecasting of production data. The analysis of transient responses of communicating wells with the new-model match to field data, an important contribution of this work, provides a basic and rigorous framework for the industry to diagnose whether wells (at least two) are communicating through fractures, and is less subjective than previous approaches.

Physical Model

Multiple horizontal wells are drilled and completed with multiple fractures in a uniform reservoir. **Fig. 3a** illustrates a system of two horizontal wells, each completed in three hydraulic-fracture stages. Branching fractures are assumed to propagate away from the primary hydraulic fractures. The primary hydraulic fractures, because they are propped, are assumed to have a higher conductivity than the branching (secondary) fractures. The secondary fractures, including activated pre-existing natural fractures, are often partially propped or unpropped, leading to their lower conductivity. As illustrated in Fig. 3a, the secondary fractures connect the isolated primary fractures of each well. Although well communication identified by "fracture hits" can occur either indirectly through secondary fractures or directly through primary hydraulic fractures, our rationale for developing the model to include the secondary-fracture case is that it gives the model more flexibility. For example, by setting the conductivity of secondary fractures to be the same as that of primary hydraulic fractures, the secondary fractures will become part of the primary-fracture system, allowing the case of interconnection between the wells through primary fractures to also be modeled. As a result, the new model can simulate different fracture geometries and conductivity distributions. All the fractures in the system can be configured with different length, conductivity, and inclination. Fully penetrating fractures are assumed, and the flow convergence to the wellbore in the primary fractures is modeled with a flow-choking skin. The following assumptions are also made:

- The reservoir is isotropic, horizontal, and of uniform thickness with impermeable lower and upper boundaries.
- Flow in the system is assumed to be single-phase flow of a slightly compressible fluid of constant viscosity.
- Reservoir fluid entering the wellbore(s) flows only through the primary fractures, and the pressure loss in the wellbore is neglected.
- Each horizontal well can be operated under different production conditions: constant rate or constant BHP.

As illustrated in Fig. 3b, the fracture system, including primary and secondary fractures, is discretized and represented by N_S segments. The intersections created by fracture interconnection are removed by use of the Star-Delta transformation. Thus, the involved fracture segments will be directly connected. The Star-Delta transformation will be discussed in a later section. The segments are numbered sequentially, from bottom-left to top-right. The discretization should capture the fracture geometry but not assume too many segments, which could slow down the simulation.

Mathematical Model

Fluid production from the reservoir is a result of flow first occurring from the matrix into the fractures, then into the wellbore(s). Neglecting pressure loss in the wellbore, there are two distinct flow processes governed by different mechanisms: matrix flow and fracture flow. In the following sections, we first describe the mathematics behind matrix and fracture flow, respectively, and then dynamically couple these two flow models by imposing continuity conditions.

Analytical Matrix-Flow Model. With the assumption of fully penetrating fractures, unsteady-state flow in the matrix will be a 2D problem. Then, single-phase fluid flow in the matrix can be expressed as

$$\frac{\partial^2 p_D}{\partial x_D^2} + \frac{\partial^2 p_D}{\partial y_D^2} = \frac{\partial p_D}{\partial t_D}, \quad (1)$$

and is subject to initial and boundary conditions.

A uniform reservoir pressure at initial conditions is assumed. During production, matrix pressure will drop because of the flow of the reservoir fluid into the discrete fracture segments. Hence, the fracture segments can be considered as planar sinks of different strengths. One of the most efficient methods to solve Eq. 1, which is subject to a number of sources/sinks, is based on the line-source function in Laplace domain. Application of the Laplace transformation with respect to time to Eq. 1 yields

$$\frac{\partial^2 \overline{p}_D}{\partial x_D^2} + \frac{\partial^2 \overline{p}_D}{\partial y_D^2} = s\overline{p}_D, \quad (2)$$

where s is a Laplace-transform variable. The dimensionless variables in Eqs. 1 and 2 are defined in Appendix A. An extensive library of Laplace-domain line-source functions for various boundary conditions has been provided by Ozkan and Raghavan (1991). In this paper, we assume that the reservoir has infinite boundaries. Finite-boundary cases, such as circular or rectangular boundaries, will be investigated in the future. For the fracture system, some fractures (secondary fractures in Fig. 3a) may not align with the x- or y-axis. **Fig. 4** shows fracture segment j with an inclination of θ_j to the x-axis with the dimensionless midpoint of (x_{Dj}, y_{Dj}).

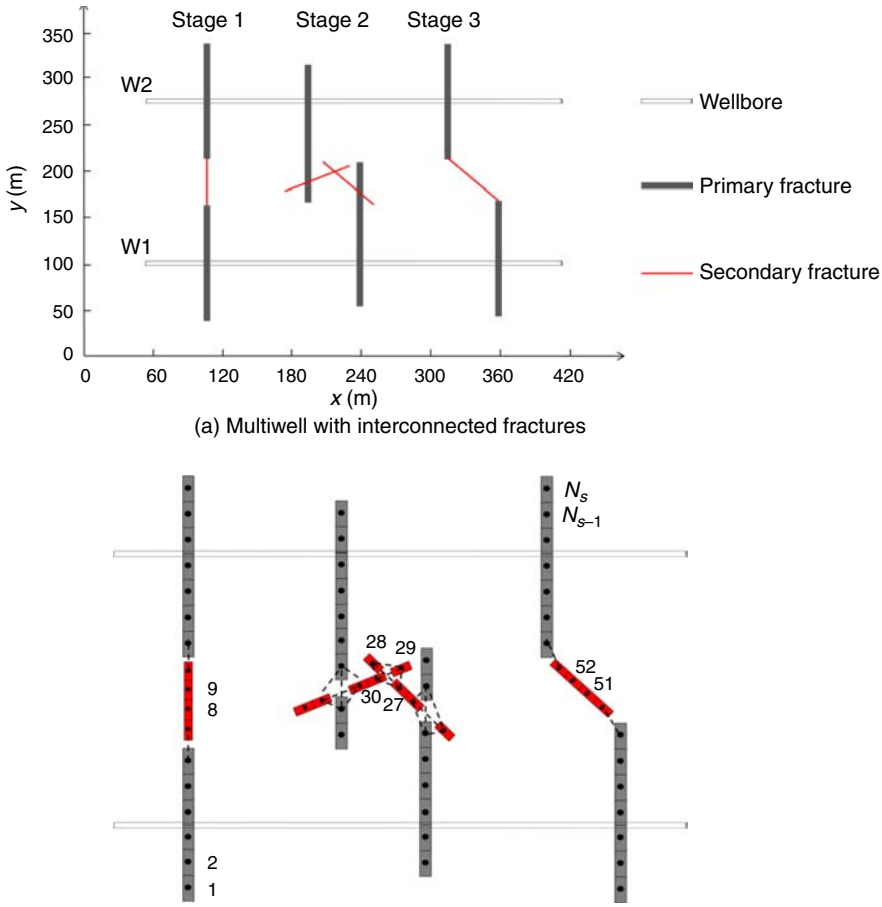

Fig. 3—Physical model for multiple wells communicating through interconnected fractures.

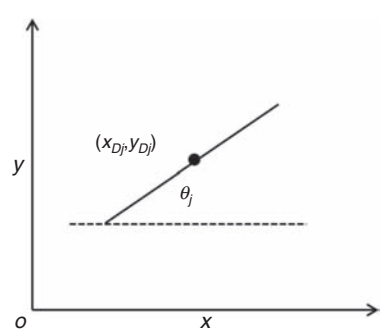

Fig. 4—Fracture segment *j* with inclination of θ_j.

Then, the dimensionless pressure in the Laplace domain at point $M(x_D,y_D)$ generated by the line-source with strength q_{Dj} is given by

$$\overline{p}_{DM} = s\overline{q}_{Dj}\overline{p}_{DM,j}, \quad (3)$$

where

$$\overline{p}_{DM,j}(x_D, y_D, s; x_{Dj}, y_{Dj}, \theta_j, \Delta L_{Dj},) = -\frac{1}{2s}\cdot \int_{-\Delta L_{Dj}/2}^{\Delta L_{Dj}/2} K_0[\sqrt{f(s)}\sqrt{(x_D - x_{Dj} - \xi\cdot\cos\theta_j)^2 + (y_D - y_{Dj} - \xi\cdot\sin\theta_j)^2}]\mathrm{d}\xi. \quad (4)$$

In Eqs. 3 and 4, $\overline{p}_{DM}$ is the dimensionless pressure in the Laplace domain at point $M(x_D,y_D)$. $\overline{p}_{DM,j}$ is the planar sink function of fracture segment j. q_{Dj} is a sink term that represents fluid flow from the matrix to the fracture segment j ($q_{Dj}=2q_j\zeta/q_r$, where q_j is the flow rate entering into segment j unit fracture length, ζ is reference length, and q_r is reference production rate). ΔL_{Dj} is the dimensionless length of segment j ($\Delta L_{Dj}=\Delta L_j/\zeta$). $f(s)$ is the transfer function in the reservoir and for the matrix, which is a single-porosity medium, $f(s)=s$. K_0 is the zeroth-order modified Bessel function of the second kind.

By use of the superposition principle, the dimensionless pressure at point M caused by N_S planar sinks (all the fracture segments in Fig. 3a) can be given by

$$\overline{p}_{DM}=\sum_{j=1}^{N_S} s\overline{q}_{Dj}\overline{p}_{DM,j}. \quad (5)$$

On the basis of Eq. 5, we can obtain the dimensionless pressure of fracture segment i:

$$\overline{p}_{Di}=\sum_{j=1}^{N_S} s\overline{q}_{Dj}\overline{p}_{Di,j}, \text{ for } i=1\cdots N_S. \quad (6a)$$

Applying Eq. 6a to the fracture system in Fig. 3a, we obtain the following linear system containing N_S equations correlating the dimensionless pressure and the dimensionless flow rate of all the fracture segments:

$$H\cdot\overline{q}_D-I\cdot\overline{p}_D=o, \quad (6b)$$

where

$$\boldsymbol{H}=\begin{bmatrix} s\overline{p}_{D1,1} & s\overline{p}_{D1,2} & \cdots & s\overline{p}_{D1,N_S} \\ s\overline{p}_{D2,1} & s\overline{p}_{D2,2} & \cdots & s\overline{p}_{D2,N_S} \\ s\overline{p}_{D3,1} & s\overline{p}_{D3,2} & \cdots & s\overline{p}_{D3,N_S} \\ & & \ddots & \\ s\overline{p}_{DN_S,1} & s\overline{p}_{DN_S,2} & \cdots & s\overline{p}_{DN_S,N_S} \end{bmatrix}, \overline{\boldsymbol{q}}_D=\begin{bmatrix} \overline{q}_{D1} \\ \overline{q}_{D2} \\ \overline{q}_{D3} \\ \vdots \\ \overline{q}_{DN_S} \end{bmatrix}, \overline{\boldsymbol{p}}_D=\begin{bmatrix} \overline{p}_{D1} \\ \overline{p}_{D2} \\ \overline{p}_{D3} \\ \vdots \\ \overline{p}_{DN_S} \end{bmatrix}, \quad (7)$$

and $\boldsymbol{I}$ is a $N_S\times N_S$ identical matrix and $\boldsymbol{o}$ is a $N_S\times 1$ zero vector.

An observation from Eq. 7 is that evaluation of the coefficient matrix, $\boldsymbol{H}$, is only related to the geometry of the fracture system, including the fracture-segment length, location, inclination, and number. It is independent of the fracture conductivity and multiwell operating conditions. This provides a better understanding of the flow behavior of multiple wells with interconnected fractures, and simplifies programming.

Numerical-Fracture Flow Model. Compared with a single well with single/multiple planar fractures, multiwell communication through interconnected fractures (as illustrated, for example, in Fig. 3a) will exhibit two different flow phenomena: One is the complex interplay of flow caused by the interconnected fractures, and the other is the multiple inner-boundary conditions introduced by multiwell production. For the discrete fracture segments illustrated in Fig. 3b, these two flow phenomena exist in the interconnected segments and segments that are adjacent to the wellbores, respectively. Here, we first derive the general form of the fracture-segment flow equation, and then discuss the approach to address the special segments. For the fracture flow, we consider unsteady-state (transient) flow in fractures. Although, wellbore-storage effects may be pronounced at early times, it is very necessary to consider the unsteady-state flow in fractures, to investigate the time to observe interference and the deviation of transient responses more accurately and theoretically. From the discussions and results, it can be concluded that the earliest time for interference is at the end of the fracture linear-flow period, when the transient-pressure pulses meet in secondary fractures. If we assume steady-state flow in the factures, then the earliest time will be at the beginning of production, because as soon as the wells produce, flow in fractures will reach a steady-state and the matrix will feed the fractures. Thus, the facture transient period will be absent. This is not considered to be realistic flow behavior of fractures.

As mentioned previously, we adopt the LTFD method to model unsteady-state flow in the fractures. Moridis et al. (1994) were the first to demonstrate the application of the LTFD method for simulation of single-phase compressible fluid flow through porous media. Habte and Onur (2014) then applied the LTFD method to investigate the transient-pressure behavior of oil/water flow associated with water-injection/falloff tests. The main feature of the LTFD method is the use of the finite-difference approach in the space discretization of the Laplace-transformed flow equation, instead of the raw equations in the real domain. Hence, it eliminates the need for time discretization, and removes the issues of stability and convergence resulting from the time discretization in conventional semianalytical or fully numerical methods. In the following section, we first present the diffusivity equation to describe the transient flow in the fractures, and then apply the Laplace transform of the equations with respect to time, and finally derive the linear system to solve for the fracture-segment pressure and flow rate.

The primary and secondary fractures are represented by finite, slab, porous media. We introduce the subscript l to facilitate the formulation derivation of fracture flow. For the flow equation of primary fractures, $l=p$, and for secondary fractures, $l=s$. Thus, the equation governing unsteady-state flow in the fracture can be given by

$$\frac{\partial^2 p_{lf}}{\partial\varepsilon^2}+\frac{\mu}{k_{lf}w_{lf}}\frac{q_{lf}(\varepsilon,t)}{h}=\frac{\phi_{lf}c_{tlf}\mu}{k_{lf}}\frac{\partial p_{lf}}{\partial t}. \quad (8)$$

The initial condition is defined by

$$p_{lf}(\varepsilon,t=0)=p_i. \quad (9)$$

The fracture tips are assumed to be closed; thus, for the closed outer-boundary condition,

$$\left.\frac{\partial p_{lf}(\varepsilon,t)}{\partial\varepsilon}\right|_{\varepsilon=\text{Tips}}=0. \quad (10)$$

If the multiwell system contains N_{CR} horizontal wells producing with constant rate, for the Ith constant-rate well with production rate q_{wI}, the inner-boundary condition can be described as

$$\left.\frac{\partial p_{pf}(\varepsilon,t)}{\partial \varepsilon}\right|_{\varepsilon=WCR_I} = -\frac{q_{wI}\mu}{k_{pf}w_{pf}h}, \text{ for } I = 1\cdots N_{CR}. \quad (11)$$

Also, if the system contains N_{CP} horizontal wells producing with constant BHP, for the Jth constant-BHP well with pressure p_{wJ}, the inner-boundary condition will be expressed as

$$p_{pf}(\varepsilon,t)|_{\varepsilon=WCP_J} = p_{wJ}, \text{for } J = 1\cdots N_{CP}. \quad (12)$$

In Eqs. 11 and 12, with the assumption that formation fluid entering wellbores flows only through the primary fractures, p_{lf} is replaced by p_{pf}. WCR_I and WCP_J represent the wellbore of the Ith constant-rate well and that of the Jth constant-BHP well, respectively.

Using the dimensionless variables defined in Appendix A and applying the Laplace transform of Eqs. 8 through 12 with respect to time, we can obtain dimensionless forms in the Laplace domain:

$$\frac{\partial^2 \overline{p}_{lfD}}{\partial \varepsilon_D^2} - \frac{\pi}{c_{lfD}}\cdot \overline{q}_{lfD}(\varepsilon_D,s) = \frac{1}{\eta_{lfD}} s\overline{p}_{lfD}. \quad (13)$$

In Eq. 13, if non-Darcy flow in fractures is considered, the approach provided by Zeng and Zhao (2010) can be used to modify the flow equation in the Laplace domain by introducing the dimensionless non-Darcy number and pseudotime.

Boundary conditions are

$$\left.\frac{\partial \overline{p}_{lfD}(\varepsilon_D,s)}{\partial \varepsilon_D}\right|_{\varepsilon_D=\text{Tips}} = 0, \quad (14)$$

$$\left.\frac{\partial \overline{p}_{pfD}(\varepsilon_D,s)}{\partial \varepsilon_D}\right|_{\varepsilon_D=WCR_I} = -\frac{1}{s}\frac{2\pi}{c_{pfD}} q_{wDI}(t=0), \text{ for } I = 1\cdots N_{CR}, \quad (15)$$

$$\overline{p}_{pfD}(\varepsilon_D,s)|_{\varepsilon_D=WCP_J} = \frac{1}{s} p_{wDJ}(t=0), \text{for } J = 1\cdots N_{CP}. \quad (16)$$

We then approximate Eqs. 13 through 16 to obtain a linear system that can be solved for dimensionless fracture pressure or flow rate. The finite-difference form of Eq. 13 is given by

$$T_{Di-1,i}\overline{p}_{lfDi-1}(s) - (T_{Di-1,i} + T_{Di+1,i} + \alpha_{Di})\overline{p}_{lfDi}(s) + T_{Di+1,i}\overline{p}_{lfDi+1}(s) - \beta_{Di}\overline{q}_{lfDi}(s) = 0, \quad (17)$$

where T_D is the dimensionless transmissibility of the adjacent segments. $T_{Di\text{-}1,i}$, α_{Di}, and β_{Di} are defined as

$$\begin{cases} T_{Di-1.i} = \dfrac{\lambda_{Di-1}\lambda_{Di}}{\lambda_{Di-1}+\lambda_{Di}}, \lambda_{Di} = \left(\dfrac{c_{lfD}}{\Delta L_D/2}\right) \\ \alpha_{Di} = s\left(\dfrac{c_{lfD}\Delta L_D}{\eta_{lfD}}\right)_i \\ \beta_{Di} = \pi\Delta L_{Di} \end{cases} \quad (18)$$

Eq. 17 is the basic form of the LTFD flow equation for the fracture segments. The form of a certain segment will change with the segment location, including the interconnected fracture segments, the segments connected to the wellbores, and the segments in the fracture tips. In the following section, the flow equation of these three types of special fracture segments will be discussed in detail.

Flow Equation of Special Fracture Segments. **Fig. 5** illustrates the scenarios of a fracture segment in fracture tips and that segment adjacent to the wellbore. These two segment types obey the boundary conditions given by Eqs. 14 through 16. For the segment in Fig. 5a, combining with Eqs. 14 and 17, we can derive the flow equation as

$$T_{Di-1,i}\overline{p}_{lfDi-1}(s) - (T_{Di-1,i} + \alpha_{Di})\overline{p}_{lfDi}(s) - \beta_{Di}\overline{q}_{lfDi}(s) = 0. \quad (19)$$

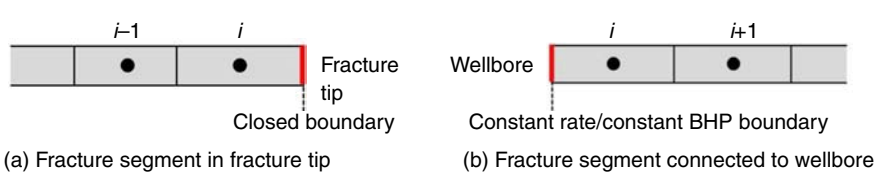

Fig. 5—Fracture segments in boundaries.

In Fig. 5b, the fracture segment is connected to the wellbore. For the case of a constant-rate well, we introduce its dimensionless BHP, which is an unknown, instead of applying the boundary condition described by Eq. 15. Eq. 15 is coupled with the matrix- and

fracture-flow equation to solve the BHP of the constant-rate well directly. Thus, if the fracture segment i is connected to the Ith constant-rate well, the finite difference form of the flow equation is given by

$$\lambda_{Di}\overline{p}_{wDI}(s) - (\lambda_{Di} + T_{Di+1,i} + \alpha_{Di})\overline{p}_{lfDi}(s) + T_{Di+1,i}\overline{p}_{lfDi+1}(s) - \beta_{Di}\overline{q}_{lfDi}(s) = 0. \quad (20)$$

In a similar way, if the fracture segment j is connected to the Jth constant-BHP well, we can obtain the finite-difference form of the flow equation by use of the boundary condition associated with Eq. 16:

$$-(\lambda_{Dj} + T_{Dj+1,j} + \alpha_{Dj})\overline{p}_{lfDj}(s) + T_{Dj+1,j}\overline{p}_{lfDj+1}(s) - \beta_{Dj}\overline{q}_{lfDj}(s) = -\frac{1}{s}\lambda_{Dj}p_{wDJ}(t=0). \quad (21)$$

For the interconnected fracture segments, the situation may be somewhat complex. **Fig. 6** illustrates two scenarios in which several fracture segments are interconnected with an intermediate intersection. To facilitate these scenarios, we assume that the interconnected fracture segments in Fig. 6b are numbered sequentially and label the intersection as cell zero. The complex interplay of flow in this situation has been comprehensively discussed in previous papers (Jia et al. 2015, 2016). In the numerical fracture-flow model, pressure of the intersection should be obtained for determination of flow redirection and flux redistribution between the interconnected fracture segments. However, in the analytical matrix-flow model, the intersection cannot be considered as line-source because of its significantly small size compared with that of the fracture segments. That is, the intersection and its unknown (pressure and flow rate) cannot be introduced into the matrix-flow model. Therefore, it will pose a problem when coupling the flow equations of the matrix-flow model and those of fracture-flow model, because of different ranks of the linear system of these two models. One of the efficient methods to tackle this situation is to remove the intersection in the fracture-flow model.

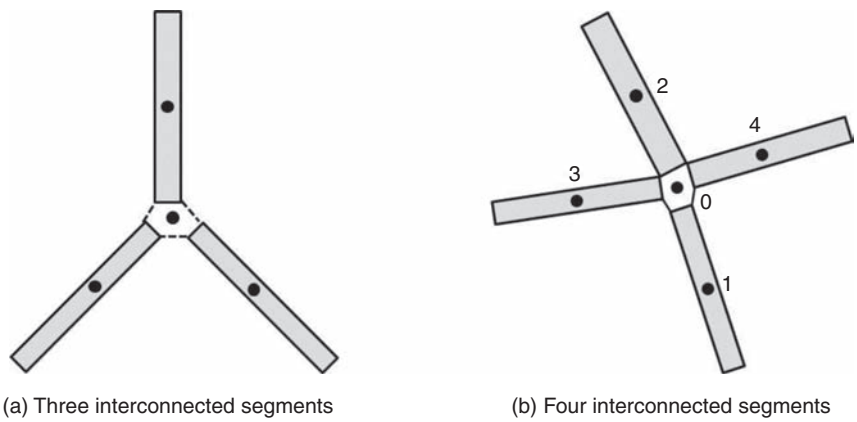

(a) Three interconnected segments (b) Four interconnected segments

Fig. 6—Examples of cases in which several fracture segments are interconnected with an intermediate intersection (modified from Jia et al. 2015).

In this paper, we adopt the Star-Delta transformation to solve the previous problem. The transformation is essentially a direct algebraic elimination of the unknown associated with the intersections that couple directly the involved fracture segments. King (1989) first used this method to evaluate the average permeability of a heterogeneous formation. Karimi-Fard et al. (2003) and Jia et al. (2015) used the approach to remove intermediate control volumes in flow simulation of discrete-fracture networks. The concept of the Star-Delta transformation for four interconnected fracture segments is illustrated in **Fig. 7.** For the case in Fig. 6b, after the transformation, the intersection is eliminated, and the involved fracture segments will be directly connected. Therefore, the transmissibility of the two arbitrary segments is given by

$$T^*_{Di,j} = \frac{T_{Di,0}T_{Dj,0}}{\sum_{k=1}^{4} T_{Dk,0}}, \quad (22)$$

where $T_{Dk,0}$ is the dimensionless transmissibility of the intersection and fracture segment k and $T_{Dk,0} = \lambda_{Dk}$. It is worth noting that Jia et al. (2015) have demonstrated that the Star-Delta transformation is also applicable to scenarios consisting of any number of interconnected fracture segments.

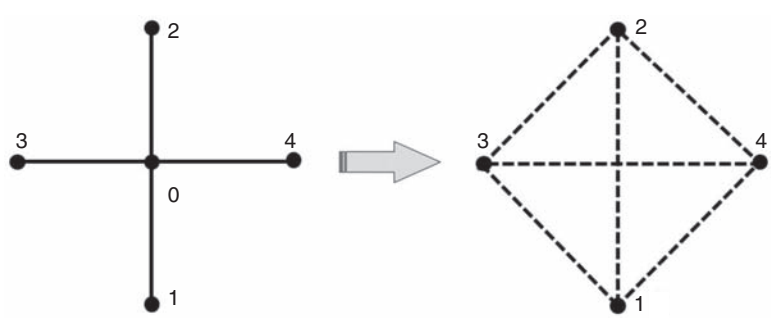

Fig. 7—Illustration of the Star-Delta transformation.

Fracture Segment 4 in Fig. 6b is used as an example of how to derive the flow equation of the interconnected fracture segments after application of the Star-Delta transformation. We assume that another fracture segment, which is adjacent to Fracture Segment 4, is numbered 5. Thus, according to Eq. 17, the flow equation of Segment 4 is expressed as

$$T_{D3,4}\overline{p}_{lfD3}(s) - (T_{D3,4} + T_{D5,4} + \alpha_{D4})\overline{p}_{lfD4}(s) + T_{D5,4}\overline{p}_{lfD5}(s) - \beta_{D4}\overline{q}_{lfD4}(s) = 0. \quad (23)$$

Eq. 23 changes to the following form after the transformation:

$$T^*_{D1,4} \cdot \overline{p}_{lfD1} + T^*_{D2,4} \cdot \overline{p}_{lfD2} + T^*_{D3,4} \cdot \overline{p}_{lfD3} - (T^*_{D1,4} + T^*_{D2,4} + T^*_{D3,4} + T_{D5,4} + \alpha_{D4}) \cdot \overline{p}_{lfD4} + T_{D5,4} \cdot \overline{p}_{lfD5} - \beta_{D4}\overline{q}_{lfD4} = 0, \quad (24)$$

where the dimensionless transmissibility $T^*_{D1,4}$, $T^*_{D2,4}$ and $T^*_{D3,4}$ can be evaluated by use of Eq. 22.

Next, for all the fracture segments in the system, on the basis of Eqs. 17 through 24, we can obtain a linear system containing N_S flow equations, which correlate the fracture-segment pressure $\overline{\boldsymbol{p}}_{lfD}$, fracture-segment flow rate $\overline{\boldsymbol{q}}_{lfD}$, and BHP $\overline{\boldsymbol{p}}_{wD}$ of N_{CR} constant-rate wells:

$$\boldsymbol{B} \cdot \overline{\boldsymbol{q}}_{lfD} + \boldsymbol{T} \cdot \overline{\boldsymbol{p}}_{lfD} + \boldsymbol{R} \cdot \overline{\boldsymbol{p}}_{wD} = \boldsymbol{b}, \quad (25)$$

where $\overline{\boldsymbol{q}}_{lfD} = [\overline{q}_{lfD1}, \cdots, \overline{q}_{lfDN_S}]^T$, $\overline{\boldsymbol{p}}_{lfD} = [\overline{p}_{lfD1}, \cdots, \overline{p}_{lfDN_S}]^T$ and $\overline{\boldsymbol{p}}_{wD} = [\overline{p}_{wD1}, \cdots, \overline{p}_{wDN_{CR}}]^T$. $\boldsymbol{B}$ is a $N_S \times N_S$ diagonal matrix, and the element on the main diagonal in row i is equal to $-\beta_{Di}$. $\boldsymbol{T}$ is a $N_S \times N_S$ sparse matrix in which all the elements are the coefficients of fracture-segment pressure, and it can be determined by Eqs. 17 through 19 and 24. $\boldsymbol{R}$ is a $N_S \times N_{CR}$ sparse matrix, and the element $\boldsymbol{R}(i,I)$ is equal to λ_{Di}, if fracture segment i is connected to the Ith constant-rate well; otherwise, the element is zero. And $\boldsymbol{b}$ is a $N_S \times 1$ vector, and the element $\boldsymbol{b}(j,1)$ will be $-\frac{1}{s}\lambda_{Dj}p_{wDJ}(t=0)$, if the fracture segment j is connected to the Jth constant-BHP well; otherwise, the element is zero.

In the previous derivations, the constant-rate boundary conditions described by Eq. 15 are not used. For the involved fracture segments, the flow equation with the constant-rate condition can be given by

$$\sum_{i \in \psi_{WCR_I}} \lambda_{Di}[\overline{p}_{lfDi}(s) - \overline{p}_{wDI}(s)] = -\frac{2\pi}{s} q_{wDI}(t=0), \text{ for } I = 1 \cdots N_{CR}, \quad (26a)$$

or

$$\sum_{i \in \psi_{WCR_I}} \lambda_{Di}\overline{p}_{lfDi}(s) + \left(-\sum_{i \in \psi_{WCR_I}} \lambda_{Di}\right)\overline{p}_{wDI}(s) = -\frac{2\pi}{s} q_{wDI}(t=0), \text{for } I = 1 \cdots N_{CR}, \quad (26b)$$

where ψ_{WCR_I} is a set which has elements that are the neighboring fracture segments of the Ith constant-rate well. Eq. 26b can be rearranged in the following matrix form:

$$\boldsymbol{R}^T \cdot \overline{\boldsymbol{p}}_{lfD} + \boldsymbol{L} \cdot \overline{\boldsymbol{p}}_{wD} = \boldsymbol{r}. \quad (27)$$

In Eq. 27, $\boldsymbol{R}$ is same as in Eq. 25. $\boldsymbol{L}$ is a $N_{CR} \times N_{CR}$ diagonal matrix, and the element on the main diagonal in row I is equal to $-\sum_{i \in \psi_{WCR_I}} \lambda_{Di}$. Finally: $\boldsymbol{r} = \left[-\frac{2\pi}{s} q_{wD1}(t=0), \cdots, -\frac{2\pi}{s} q_{wDN_{CR}}(t=0)\right]^T$.

Solution of Transient Responses. Transient responses are obtained by coupling the analytical matrix-flow model and the numerical fracture-flow model, along with the constant-rate boundary conditions. Because of the continuity of pressure and flow rate on the fracture surface, the following conditions must be imposed on each fracture segment:

$$\begin{cases} p_{lfD} = p_D \\ q_{lfD} = q_D \end{cases} \quad (28)$$

Then, combining Eqs. 6a, 25, and 27 generates a $(2\,N_S + N_{CR}) \times (2\,N_S + N_{CR})$ linear system to be solved for the fracture-segment pressure $\overline{\boldsymbol{p}}_{lfD}$, fracture-segment flow rate $\overline{\boldsymbol{q}}_{lfD}$, and BHP $\overline{\boldsymbol{p}}_{wD}$ of N_{CR} constant-rate wells:

$$\begin{bmatrix} \boldsymbol{H} & -\boldsymbol{I} & \boldsymbol{O} \\ \boldsymbol{B} & \boldsymbol{T} & \boldsymbol{R} \\ \boldsymbol{O}^T & \boldsymbol{R}^T & \boldsymbol{L} \end{bmatrix} \cdot \begin{bmatrix} \overline{\boldsymbol{q}}_{lfD} \\ \overline{\boldsymbol{p}}_{lfD} \\ \overline{\boldsymbol{p}}_{wD} \end{bmatrix} = \begin{bmatrix} \boldsymbol{o} \\ \boldsymbol{b} \\ \boldsymbol{r} \end{bmatrix}, \quad (29)$$

where $\boldsymbol{O}$ is a $N_S \times N_{CR}$ zero matrix. Eq. 29 can be solved with the Gauss elimination method. Appendix B provides the detailed derivation of Eq. 29. Then, production rate of the Jth constant-BHP well can be calculated by

$$\overline{q}_{wDJ} = \frac{1}{2\pi} \sum_{j \in \psi_{WCP_J}} \lambda_{Dj}\left[\frac{1}{s}p_{wDJ}(t=0) - \overline{p}_{lfDj}(s)\right], \text{for } J = 1 \cdots N_{CP}, \quad (30)$$

where ψ_{WCP_J} is a set which has elements that are the neighboring fracture segments of the Jth constant-BHP well.

Finally, the transient pressure and rate of the multiwell communication system in the real domain can be obtained by applying the Stehfest numerical-inversion algorithm (Stehfest 1970). In the algorithm, the approximate value of the inverse function is evaluated by the summation of the Laplace transform of the inversion function. The number of the summation, N, must be even. Theoretically, the approximate value becomes more accurate for greater values of N. Practically, however, rounding errors worsen the results if N becomes too large. For the problem of flow in porous media (diffusivity equation in this study), the optimal value range of N is 4 through 16. A sensitive analysis of N was conducted, and it was found that with $N = 8$, the results can achieve a relative error of 10^{-5}. In this study, we therefore adopt $N = 8$.

Model Modifications

Following the work of Stalgorova and Mattar (2013), we provide some possible model modifications to extend the model to consider the gas flow, flow choking, and the wellbore-storage effect.

Gas Flow. The assumptions used in the Physical Model section are mainly for single-phase liquid flow. For gas flow, the diffusivity term is varying with pressure, so the governing flow equation becomes nonlinear. The common way to deal with the problem is to use pseudotime (Anderson and Mattar 2005) to linearize the equation. Furthermore, the pressure-dependent properties can also be incorporated in our hybrid model by use of modified pseudopressure (Clarkson et al. 2012; Qanbari and Clarkson 2012).

Flow Choking and Wellbore-Storage Effect. In the previous derivation, we assume 1D flow in the fractures to neglect the flow convergence to the wellbore in the primary fractures. This convergence often results in an additional pressure drop. The common way to account for this effect is to adopt the flow-choking skin factor provided by Mukherjee and Economides (1991):

$$s_c = \frac{k_m h}{k_{pf} w_{pf}} \left[\ln\left(\frac{h}{2r_w}\right) - \frac{\pi}{2} \right]. \quad (31)$$

Then, flow-choking skin along with wellbore-storage effect can be incorporated into the solution for a constant-rate well by use of the following equation derived by Van Everdingen and Hurst (1949):

$$\overline{p}_{wD,\text{skin,storage}} = \frac{s\overline{p}_{wD} + s_c}{s + C_D s^2 (s\overline{p}_{wD} + s_c)}. \quad (32)$$

Eq. 32 can also be applied to the transient-rate response of a constant-BHP well.

Considerations for Computation

A computer program was written to solve Eqs. 29 through 31. Discrete times can be predetermined with Laplace-domain solutions. The computation performance, including the accuracy of the results and the computation time required for the hybrid model, is mainly dependent on the fracture-discretization issues and the numerical evaluation of the integral in Eq. 4. As for the numerical fracture-flow model, the choice of an appropriate segment system is essential for the accuracy of the fracture-flow simulation. In our computations, we use unequal-length segments to describe the fractures, and adopt refined segments for the fracture segments close to intersections. A concern is that flow rate q_{lfD} of the fracture segments close to the intersections will change greatly, relative to other sections, because of stronger pressure interference in the matrix, surrounding the intersections. Therefore, finer grid spacing for the segments close to the intersections can guarantee a uniform distribution of flow rate in each segment, as far as possible. A sensitivity analysis was conducted to investigate these effects. It was found that the solutions do not change appreciably when more than six segments are used along the length of facture that is separated by two intersections.

Numerical evaluation of the integral in Eq. 4 will determine the speed of the computation and the accuracy of matrix-flow simulation. In the program, we use the adaptive quadrature method to evaluate the integral. The convergence is dominantly influenced by the Laplace variable, s (i.e., the dimensionless time caused by $s = i\ln 2/t_D$ in the Stehfest numerical-inversion algorithm). According to our analysis, the integrand in Eq. 4 of each fracture segment should be evaluated approximately 300 times to achieve a relative error of 10^{-5} when $t_D = 10^{-6}$. The number of evaluations will decrease to approximately 25 and 10 for $t_D = 10^{-2}$ and 10^2, respectively, with the same tolerance. Therefore, in the program, a relative error of 10^{-5} is used as the criterion for convergence of the integral in Eq. 4. In addition, the numerical evaluation of the integral will pose another problem if i is equal to j and θ_i is zero or $\pi/2$ in $\overline{p}_{Di,j}$: The function K_0 will encounter a singular point. As Ozkan and Raghavan (1991) suggested, this problem can be eliminated completely if we adopt the following alternative forms for Eq. 4. For example, when a θ_i is equal to zero, we can recast

$$\overline{p}_{Di,i} = -\frac{1}{2s} \cdot \int_{-\Delta L_{Di}/2}^{\Delta L_{Di}/2} K_0\left[\sqrt{f(s)}\sqrt{\xi^2}\right] \mathrm{d}\xi, \quad (33)$$

as

$$\begin{aligned}\overline{p}_{Di,i} &= -\frac{1}{2s} \cdot \left\{ \int_{-\Delta L_{Di}/2}^{0} K_0\left[-\sqrt{f(s)}\xi\right] \mathrm{d}\xi + \int_{0}^{\Delta L_{Di}/2} K_0\left[\sqrt{f(s)}\xi\right] \mathrm{d}\xi \right\} \\ &= -\frac{1}{2s} \cdot 2\int_{0}^{\Delta L_{Di}/2} K_0\left[\sqrt{f(s)}\xi\right] \mathrm{d}\xi. \quad (34)\end{aligned}$$

Integrals on the right side of Eq. 34 can now be computed without difficulty with the adaptive quadrature method.

Model Validation

In this section, the hybrid model is validated. The model-validation study is conducted by comparing the dimensionless pressure, derivative, and rate signatures from our model with the results of the Eclipse™ numerical simulator and the semianalytical model developed by Yu et al. (2016). **Fig. 8** illustrates the fracture geometry and dimensions of the examples used for verification.

Validation Against Fully Numerical Model. In the fully numerical model built in Eclipse, the global grid system with the grid configuration of $117 \times 96 \times 1$ is shown in **Fig. 9.** The space surrounding the fractures is discretized logarithmically, ranging from 0.01 to 5.84 m, to ensure that the grids near the fractures are refined enough to capture accurate flow behavior. The grids with a width of 0.01 m, indicated by solid red lines, are assigned a different permeability to represent primary and secondary fractures with different conductivities. With the assumption of closed fracture tips, the fracture-segment transmissibility in the flow direction from fracture tips is set to zero. The fluid is assumed to be a single-phase black oil with very low bubblepoint to ensure single-phase flow in the reservoir throughout production life. The well labeled 'W1" produces under a constant-rate condition, and the "W2" well produces under a

constant-BHP condition. **Table 1** provides the input data used for the comparison. In the hybrid model, we adopt 60 ($N_S = 60$) fracture segments and 10 discrete times in each log-cycle to simulate the same system.

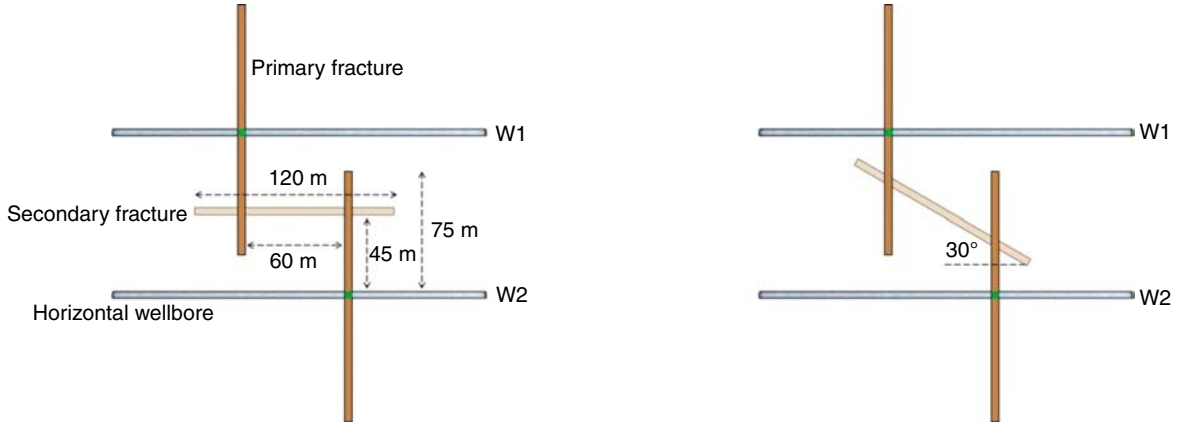

(a) Example used for verification with fully numerical model (b) Example used for verification with the semi-analytical model

Fig. 8—Fracture geometry and dimensions used for model-verification examples. The difference between (a) and (b) is the secondary-fracture inclination. In (b), the secondary fracture has an inclination of 30° to the horizontal direction.

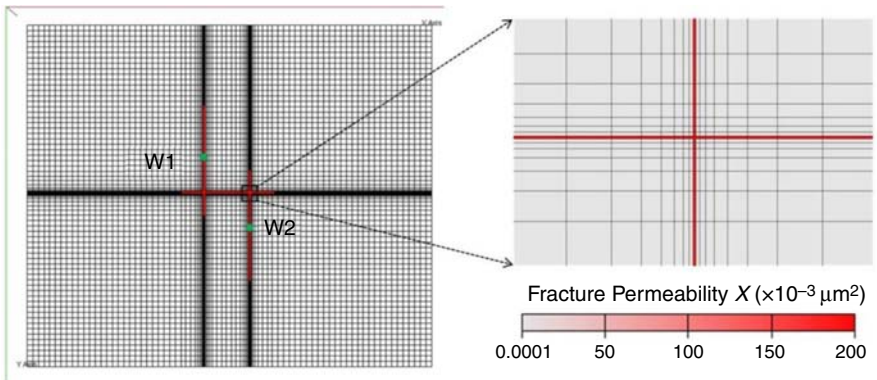

Fig. 9—(Left) top view of the global grid configuration used in fully numerical model. (Right) A view of locally interconnected fractures and surrounding matrix grids with permeability distribution in *x*-direction. The permeability distribution in *y*-direction is the same as that in *x*-direction.

Well, Reservoir, Fluid, and Fracture Data

Formation thickness, h (m)	60	Oil formation volume factor, B (m^3/m^3)	1.1
Initial pressure, p_i (MPa)	30	Wellbore-storage coefficient, C (m^3/MPa)	0
Wellbore radius, r_w (m)	0.1	Choking-skin factor, S	0.00947
Matrix permeability, k_m ($\times 10^{-3}\mu m^2$)	1×10^{-4}	Reference length, ζ (m)	80
Matrix porosity, ϕ_m	0.05	Reference rate, q_r (m^3/d)	0.1
Matrix compressibility, c_{tm} (MPa^{-1})	4×10^{-4}	Production rate of W1, q_w (MPa)	0.1
Primary-fracture permeability, k_{pf} ($\times 10^{-3}\mu m^2$)	500	BHP of W2, p_w (MPa)	5
Primary-fracture width, w_{pf} (m)	0.01	Dimensionless primary-fracture conductivity, c_{pfD}	628.57
Primary-fracture porosity, ϕ_{pf}	0.46	Dimensionless primary-fracture diffusivity, η_{pfD}	3.26×10^4
Primary-fracture compressibility, c_{tpf} (MPa^{-1})	7.25×10^{-3}	Dimensionless secondary-fracture conductivity, c_{sfD}	7.62
Secondary-fracture permeability, k_{sf} ($\times 10^{-3}\mu m^2$)	60	Dimensionless secondary-fracture diffusivity, η_{sfD}	5.56×10^3
Secondary-fracture width, w_{sf} (m)	0.01	Dimensionless production rate of W1	1
Secondary-fracture porosity, ϕ_{sf}	0.54	Dimensionless BHP of W2	0.93
Secondary- fracture compressibility, c_{tsf} (MPa^{-1})	1.45×10^{-3}	Dimensionless wellbore-storage coefficient, C_D	0
Fluid viscosity, μ (mPa.s)	0.8	Number of fracture segment, N_S	60

Table 1—Data used for model validation.

Fig. 10 provides a comparison of the results of the fully numerical model and the hybrid model for the example in Fig. 8a and Fig. 9. The curves are in excellent agreement, except for the pressure responses of W1 and the rate of W2 at very early time. This may be caused by the different approaches to deal with the early-time radial flow to wellbore in the primary fractures. In the fully numerical model, the radial flow will develop in the grid in which the well is completed. However, the flow-choking skin is used in our hybrid model. This will create different skin factors for the flow convergence to the wellbore. The derivative of pressure vs. time is independent of the constant skin factor. Therefore, transient-derivative responses of the two models are in agreement for the whole well life.

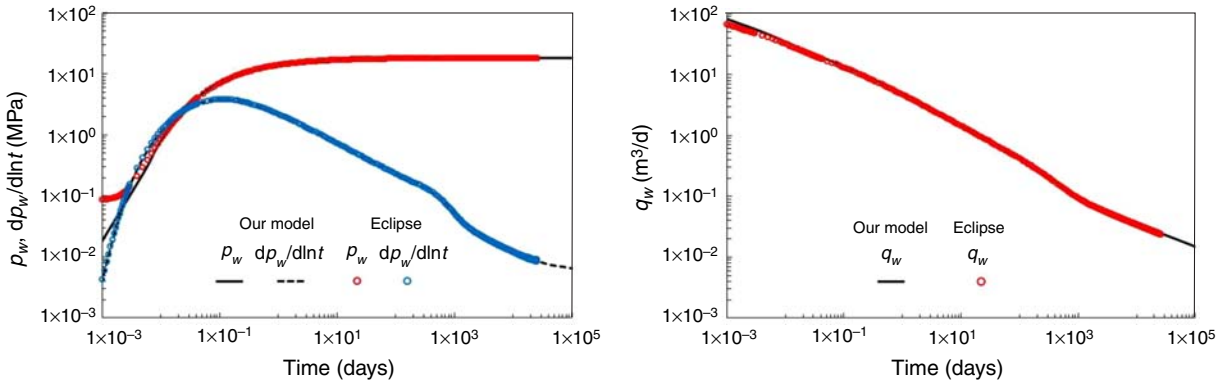

(a) The transient pressure and derivative of W1

(b) The production rate of W2

Fig. 10—Comparison of the results of our hybrid model and fully numerical model.

In addition, the speed of the computations for our hybrid model and Eclipse simulator is compared with the same hardware platform. For the previous simulations, the computation times are 16.5 and 19.1 seconds for the model in this paper and the numerical model, respectively. The improvement of computation performance is therefore not significant for the cases studied. However, we suggest that this comparison is not a compete test of the new model speed vs. full numerical simulation caused by the fracture geometry (orthogonal) and number of fractures (three fractures) and the program used (Matlab codes without optimization) in the validation example. The improvement may be considerable for the case with complex-fracture network or some improved-programming efficiency.

Validation Against Semianalytical Model. With the example in Fig. 8b, we compare the new model against the semianalytical model developed by Yu et al. (2016). W1 and W2 are operated with a constant BHP of 6 and 5 MPa, respectively. Addition input data are provided in Table 1. **Fig. 11** provides a comparison of the rate of our model and the semianalytical model. It can be seen that the deviations of the results occur mainly at early time. In the early-time period, the results of the new model exhibit a fracture linear-flow period (1/2 slope marked by the dashed red line), followed by a bilinear-flow period (1/4 slope marked by the dashed blue line), whereas the semianalytical model exhibits a bilinear-flow period for the same time interval. This may be because of the different approaches used to model fracture flow. In the new hybrid model, we consider unsteady-state flow in fractures. The system should exhibit a fracture linear flow after the wells start producing. However, in the model of Yu et al. (2016), steady-state flow is considered in the fractures. As soon as the wells produce, flow in fractures will reach steady-state instantaneously, and the matrix will feed the fractures. Hence, the fracture linear-flow period will be absent for the Yu model, and bilinear flow will develop instantly. The deviations of both models will increase with a larger fracture length and lower fracture conductivity. It is necessary to consider unsteady-state flow in fractures to capture the early flow behavior rigorously, such as required for the determination of response time and pressure caused by fracture interference (Awada et al. 2016). An additional benefit of the hybrid model is that it saves 10.3 seconds in computation time compared with the semianalytical model.

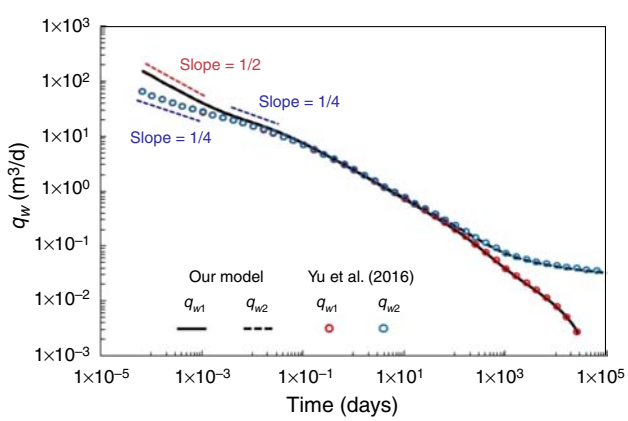

Fig. 11—Comparison of the results of the new hybrid model and the model of Yu et al. (2016).

Results and Discussion

In the following sections, we first investigate the flow behavior of a simple example that contains two wells with a single primary fracture for each well corresponding to Stage 1 shown in Fig. 3a. The purpose is to analyze the difference between the results of the noncommunicating case and those of the communicating case under different production conditions. Next, we investigate the effect of

secondary-fracture conductivity, the number of connections, and communicating well-operating conditions on well performance with multiple fractures communicating through complex secondary fractures (as shown in Fig. 2a). Well interference is a primary result of multiwell communication. In Awada et al. (2016), the time to observe interference is referenced to the point when a pressure deviation of 0.1 MPa is observed for the constant-rate wells. Alternatively, we adopt a relative pressure/rate deviation of 1×10^{-5} as the criterion for the time to observe interference. Our logic is that a relative deviation provides a more reasonable analysis of pressure/rate change through the well life. Although this approach to determine the interference may be somewhat subjective, it can provide a reasonably accurate evaluation of the time for interference to be observed.

Single Primary-Fracture Communication Through One Secondary Fracture. As shown in Fig. 3a (Stage 1), the two isolated primary fractures are communicating through a secondary fracture. This initial example is taken as the basic communicating case. For the corresponding noncommunicating case, we set the transmissibility of the middle part of the secondary fracture (e.g., the transmissibility between fracture Segments 8 and 9 in Fig. 3b) to zero. This ensures that the comparison can be conducted with the same fracture geometry. Practically, the primary fractures (propped fracture) have a $45 \times 10^{-3}\mu m^2 \cdot m$ conductivity, whereas the secondary fracture (unpropped fracture) is configured with a $1.5 \times 10^{-3}\mu m^2 \cdot m$ conductivity (Cipolla et al. 2010). Three production strategies listed in **Table 2** are investigated. Additional data are provided in Table 1.

Production Strategy	W1	W2
P1 (W1 constant rate and W2 constant rate)	0.5 m^3/d	2 m^3/d
P2 (W1 constant BHP and W2 constant BHP)	10 MPa	5 MPa
P3 (W1 constant rate and W2 constant BHP)	0.5 m^3/d	5 MPa

Table 2—Different production strategies.

For Production Strategy P1, the total production rate $(q_{w1} + q_{w2})$ is set as the reference rate for the dimensionless variables. **Fig. 12** provides a comparison of dimensionless pressure and derivative for the communicating and noncommunicating cases. **Fig. 13** plots pressure distribution of fracture segments between the two wells to facilitate analysis of communication behavior. It can be seen that, for a noncommunicating case, the wells both develop fracture-linear and matrix-linear flow periods (marked by black dots in Fig. 12a), and the different response levels are caused by the different production rate of each well. Bilinear flow is absent because of high-conductivity primary fractures. When the two wells communicate through the secondary fracture, the responses deviate from those of the noncommunicating case at the end of the transient flow period (marked by red dots in Fig. 12b). The time for the observed deviation is obtained by use of the pressure-change point defined in the previous section. After this, as shown in Fig. 12, the pressure interference between the communicating wells will take effect, and the curves of W1 exhibit an upward trend whereas the curves of W2 exhibit a downward trend. As time increases, the responses of the two wells gradually converge, and the combined response appears as if one well is producing from the two combined primary fractures. A short matrix linear-flow period will develop at this point.

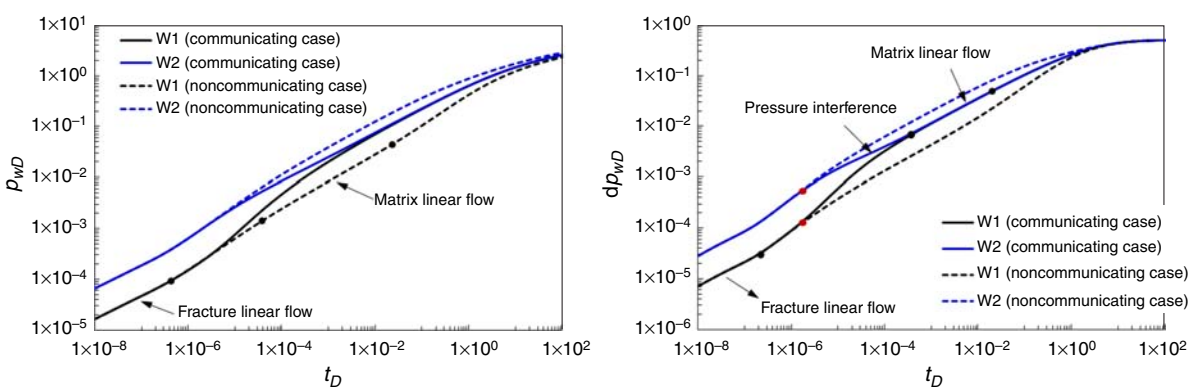

(a) Dimensionless pressure curves (b) Dimensionless derivative curves

Fig. 12—Comparison of transient responses of the communicating and noncommunicating multiwell cases with the P1 production strategy.

These results can be explained as follows. When the pressure pulses from the two wells touch in the secondary fracture, the primary-fracture tip pressure of the low-rate well (W1) is higher than that of the high-rate well (W2)—refer to the fracture-pressure profile at $t_D = 6 \times 10^{-7}$ in Fig. 13a. Therefore, when the secondary-fracture pressure is lower than the primary-fracture pressure of W1, W2 will also be sourced by the primary fracture of W1, including fluid sourced from matrix. The source that will dominate is dependent on the pressure difference between the two primary fractures and the flow resistance in the connected facture (i.e., the production-rate difference, and the secondary-fracture conductivity, for a given fracture geometry). If matrix source is dominant, the contribution from communication can be neglected, and then the transient-response deviation will be delayed, which is difficult to observe in some cases. Otherwise, the deviation will be evident instantly (i.e., that pressure interference will take effect). In this example, the pressure interference is observed at the end of the transient flow period. This can be clearly illustrated by the descending trend of secondary-fracture pressure, toward W2 when $t_D = 2 \times 10^{-6}$ in Fig. 13a. Thus, the responses of W2 will exhibit a downward trend, and accordingly, an upward trend for the curves of W1. As time increases, the flow in the fractures will stabilize, and the merged curves exhibit matrix linear flow. The equivalent wellbore pressures of the two wells at $t_D = 5 \times 10^{-2}$ in Fig. 13b support this observation. The interference time is approximately 14.5 minutes for the results shown in Fig. 12. This very early interference time is also found by Awada et al. (2016), for a multiwell case connected through a fracture network.

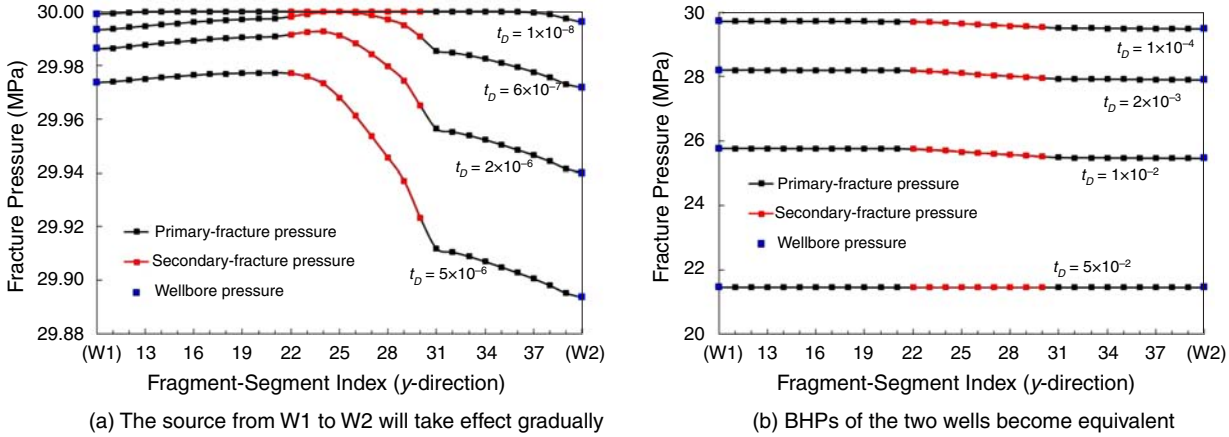

(a) The source from W1 to W2 will take effect gradually

(b) BHPs of the two wells become equivalent

Fig. 13—Wellbore and fracture pressure distribution of the communicating-well case with the P1 production strategy.

Fig. 14 illustrates the dimensionless rate curves of the communicating and noncommunicating cases with the P2 production strategy. As with the P1 production strategy, the two wells without communication exhibit a fracture linear-flow period and a matrix linear-flow period. For the communicating case, the rate deviation occurs during the matrix linear-flow period, and the response time for interference is approximately 54 minutes with a relative rate deviation of 1×10^{-5}. Before the interference, the system exhibits a fracture linear flow followed by a short matrix linear-flow period. This can also be deduced for the fracture-pressure distribution at $t_D = 2 \times 10^{-5}$, shown in **Fig. 15a.** At this time, fracture sourcing from W1 to W2 will become dominant; thus, pressure interference takes effect. In contrast to the behavior of the two constant-rate wells, the transient responses will deviate greatly with production for these two communicating constant-BHP wells, instead of merging to develop matrix linear flow. The reason may be that after interference is observed, the primary-fracture pressure of high-BHP well (W1) will always be higher than that of low-BHP well (W2), as illustrated in Fig. 15b; therefore, the primary fracture of W1 will source W2 throughout the production life. As time increases, when the pressure of the primary-fracture segment connected to the wellbore of W1 is lower than the BHP of W1, the production rate of W1 will be negative. and W1 becomes an injection well. In Fig. 15b, at $t_D = 1 \times 10^{-1}$, the pressure of the fracture segment numbered 11 (connected to W1 wellbore) is 9.995 MPa, which is lower than the BHP of W1 (10 MPa). This indicates that W1 already has a negative production rate at this time. For field cases, a negative rate for a production well is obviously unrealistic. If a well is this negatively affected, it would be shut in after it reaches an economic limit rate. However, the previous theoretical analysis suggests that if two wells are connected by fractures, one well will suffer production loss caused by interference through the interconnected fractures. These findings are consistent with those of Lawal et al. (2013, who noted rate loss of a producing well caused by a neighboring well hydraulically interacting with it.

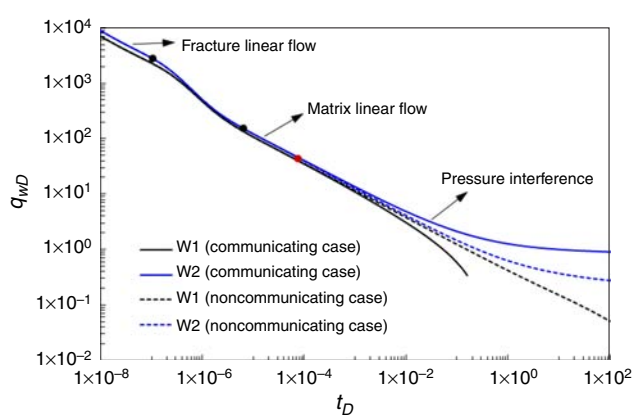

Fig. 14—Comparison of transient responses of the communicating and noncommunicating multiwell cases with the P2 production strategy.

Fig. 16 illustrates the dimensionless pressure, derivative and rate responses of the communicating and noncommunicating case with the P3 production strategy. Without communication, the two wells all develop a fracture and matrix linear-flow period. However, although these two isolated wells are not connected by fractures, interference through the matrix is evident and can be diagnosed by the downward trend of the dimensionless derivative of W1, and a sharp decline of production rate of W2, at the later time. For the communicating case, the situation is more complex. Before interference, a fracture linear-flow period is followed by a short matrix linear-flow period. When pressure interference takes effect, the primary-fracture pressure of the constant-rate well (W1) is often higher than that of the constant-BHP well (W2), caused by high primary-fracture conductivity. Therefore, W2 is first sourced by the primary fracture of W1. In this example, the fracture sourcing will become dominant during the matrix linear-flow period (approximately 40 minutes). The fracture-pressure distribution at $t_D = 2 \times 10^{-6}$ in **Fig. 17** clearly supports this statement. As shown in Fig. 17, the primary-fracture pressure of W1 decreases with production, and, after a certain time, the pressure is lower than that of W2. Next, W1 will be sourced by W2, and the rate of W2 will exhibit a sharp decline and reach a negative rate.

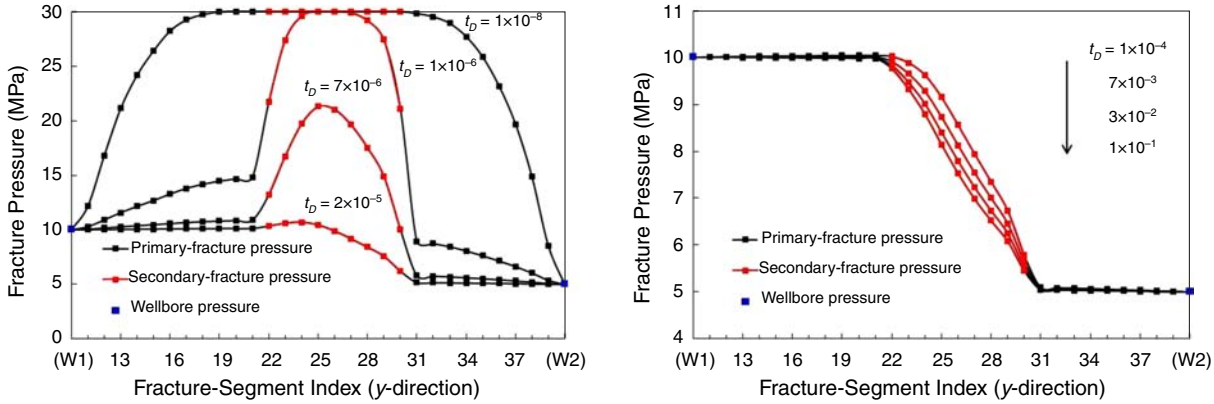

(a) The source from W1 to W2 will take effect gradually

(b) W1 always sources W2 after interference

Fig. 15—Wellbore and fracture-pressure distribution of the communicating-well case with the P2 production strategy.

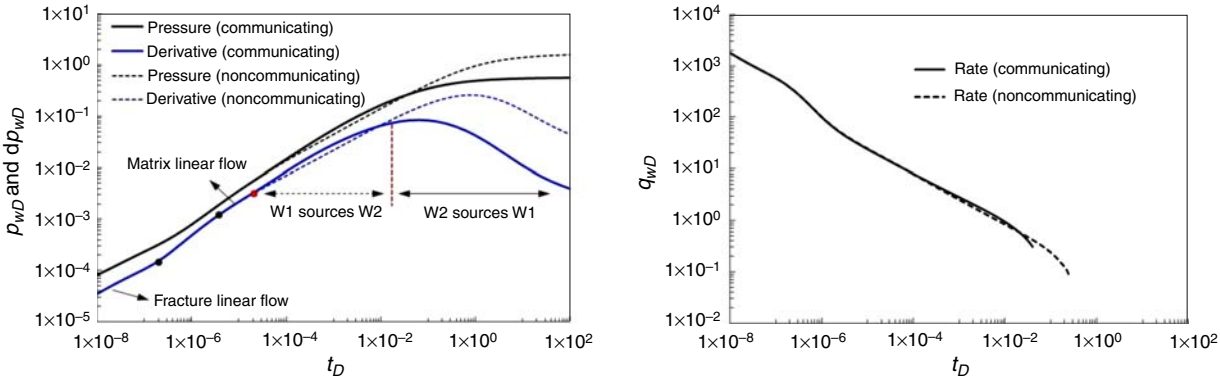

(a) Dimensionless pressure and derivative of W1

(b) Dimensionless rate of W2

Fig. 16—Comparison of transient responses of the communicating and noncommunicating multiwell cases with the P3 production strategy.

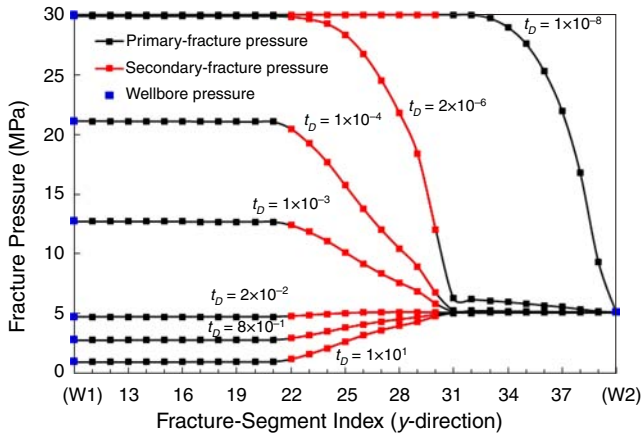

Fig. 17—Wellbore and fracture pressure distribution of the communicating-well case with the P3 production strategy.

In the previous discussion, it is observed that a primary characteristic of the multiwell production behavior is pressure interference through fracture communication. Before interference, the communicating wells behave as single isolated wells. Therefore, the fracture linear flow and matrix linear flow will develop during the noncommunicating period. The end time of matrix linear flow may be affected by fracture conductivities and operation conditions, whereas fracture linear flow will not be disturbed. It should be noted that we selected an appropriate set of parameters to illustrate all possible flow regimes, which may not exist in a single simulation. Depending on the properties of the system, including fracture conductivity, fracture geometry and well production conditions, some flow regimes may be absent.

Multiple Primary-Fracture Communication Through Complex Secondary Fractures. In this subsection, we focus on the effect of secondary-fracture conductivity, number of connections, and operating conditions on the flow behavior of multiple communicating wells by use of the system in Fig. 3a. As illustrated in Fig. 3a, the number of connections, N_C, is three. To decrease N_C, we set the transmissibility between certain fracture segments, such as the sets of (8,9), (10,11,12,13), and (15,16) in Fig. 3b to zero. Therefore, the

effect of the number of connections can be investigated with the same fracture geometry. The analysis is conducted with three different production strategies, such as the ones in Table 2. Additional input data are provided in Table 1. The investigated parameters are provided in dimensionless form in the associated figures.

Two Constant-Rate Wells. **Fig. 18a** illustrates the effect of secondary-fracture conductivity on the dimensionless pressure of two communicating wells under constant-rate conditions. The example with $c_{sfD} = 400$ is designed as a case with infinite-conductivity secondary fractures, and when $c_{sfD} = 4 \times 10^{-5}$, the permeability of secondary fracture is the same as that of the matrix. It can be seen that secondary-fracture conductivity significantly alters the flow signature compared with single (isolated) wells. The times to observe interference for the first four cases ($c_{sfD} = 400$, 40, 4, 0.4) are 1.6, 6.2, 61.9, and 981.4 minutes, respectively. With a decrease in secondary-fracture conductivity, the interference is delayed, and the duration of the matrix linear-flow period developed before interference is therefore prolonged. In these cases, the transient responses of the two wells will converge at a very late time, and matrix linear flow may be absent. In addition, we find that, even with infinite-conductivity secondary fractures, the fracture linear flow is not affected. This is mainly because the observed interference occurs later than pressure pulses touching from the wells, which is at the end of the fracture linear-flow period.

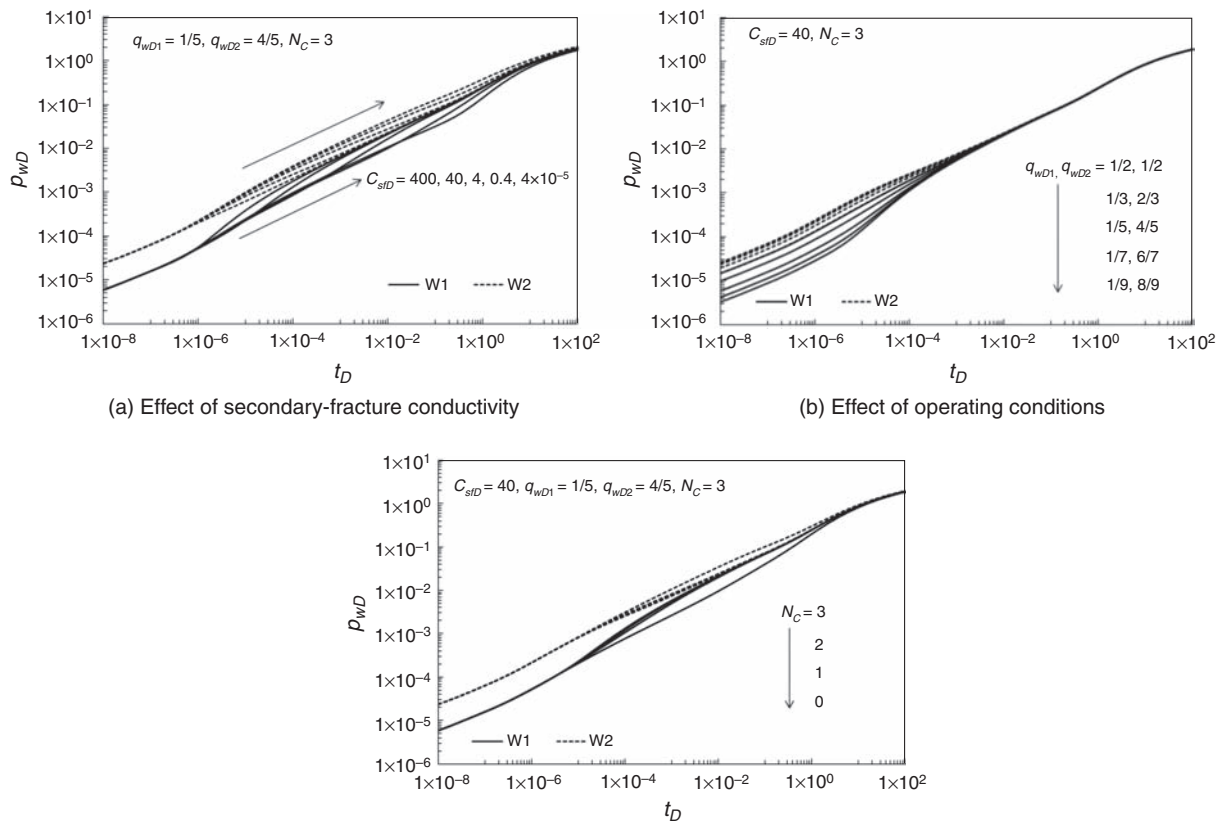

Fig. 18—Effect of key parameters on the transient responses of two communicating constant-rate wells.

The effect of operating conditions is illustrated in Fig. 18b. The influence is primarily on fracture linear flow and subsequent transient flow periods. The matrix linear-flow period caused by the transient responses merging is hardly affected. The reason for the difference between dimensionless pressures in the fracture linear-flow period is that interference has not occurred during this period, and pressure is only related to the rate for a given fracture system. The interference times for these cases, from small to large contrast in production rates, are 21.4, 9.8, 6.2, 5.7, and 5.5 minutes, respectively. With an increase in rate contrast, the pressure difference of the primary-fracture tip of the wells is increased. The time response caused by interference is therefore advanced. However, the effect is not as important as secondary-fracture conductivity. From the results of Fig. 18c, we can see that after the two isolated wells communicate through fractures, the flow behavior is altered significantly. The interference times for $N_C = 1$, 2, 3 (6.2, 9.1, and 24.5 minutes) suggest that a larger number of connections will cause an earlier interference. However, the effect on the transient-responses curves is not evident.

Two Constant-BHP Wells. As illustrated in **Fig. 19a,** the effect of secondary-fracture conductivity on flow behavior is also significant for two communicating constant-BHP wells. As the transient responses of the case with infinite-conductivity secondary fractures ($c_{sfD} = 400$) suggest, secondary-fracture conductivity hardly influences the fracture linear-flow period. With an increase in c_{sfD}, the interference will be advanced, and the duration of matrix linear-flow period becomes shorter. Hence, if the two constant-BHP wells are connected by high-conductivity fractures, the rate loss of the higher BHP well occurs very early, and the production rate of the negatively affected well will decline sharply. In Fig. 19b, we investigate the effect of operating conditions by changing the BHP of W1. For practical purposes, the dimensionless BHPs of 0.4, 0.6, 0.8, 0.9, and 1.0 correspond to 20, 15, 10, 7.5, and 5 MPa, respectively, by use of the basic data in Table 1. It can be seen that a lower-dimensionless-BHP generates a lower production rate and advanced interference. Therefore, the lower dimensionless BHP well (W1) will exhibit a shorter matrix linear-flow period and an accelerated rate decline. This is mainly because, with a large contrast of BHPs of the two communicating wells, the pressure difference of the primary fractures of the two wells will increase and the fluid sourced from W1 to W2 will therefore become dominant earlier. The influence of

the number of connections is shown in Fig. 19c. For the case of $N_C = 0$, a long matrix linear-flow period is observed, and the sharp decline of W1 rate indicates that the pressure interference is still occurring through matrix. With increasing N_C, the interference time is advanced. However, the rate deviation caused by interference has little effect on the duration of the matrix linear-flow period.

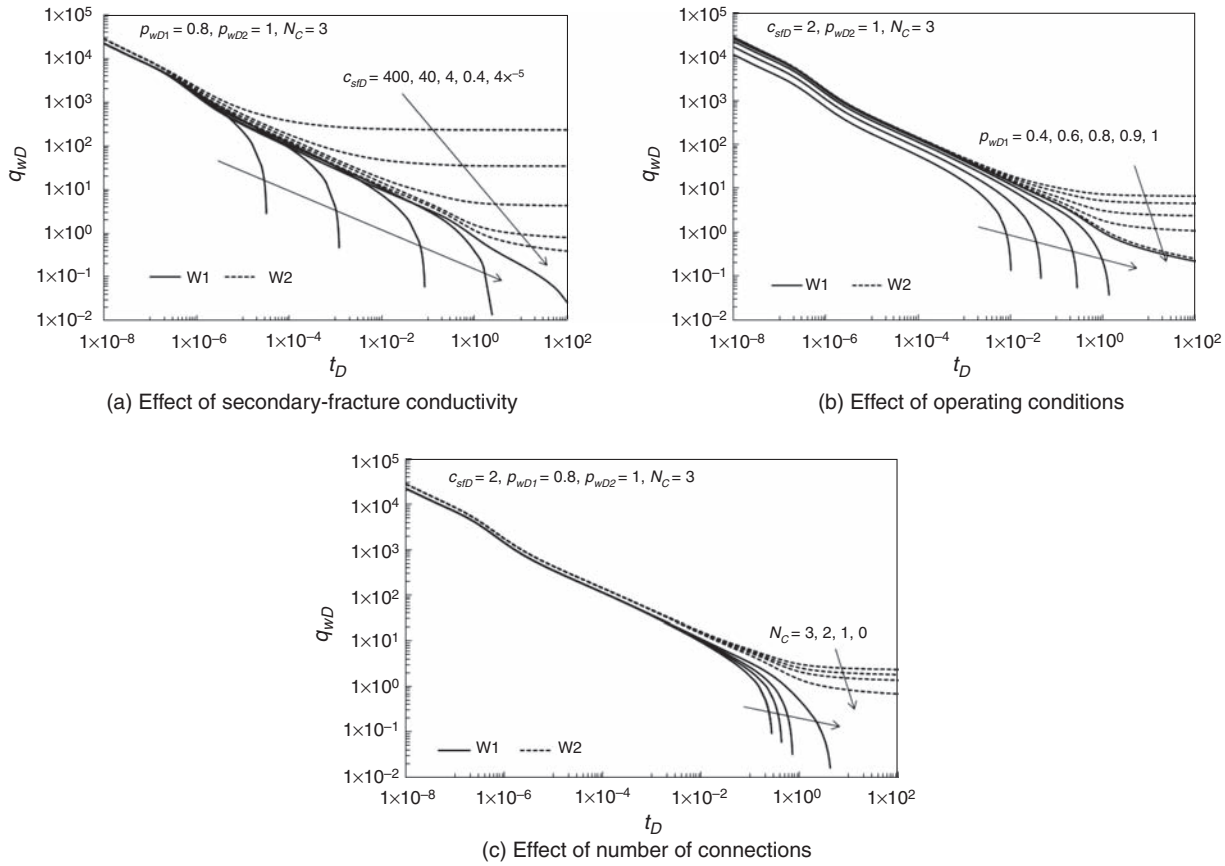

Fig. 19—Effect of key parameters on the transient responses of two communicating constant-BHP wells.

One Constant-Rate Well and One Constant-BHP Well. From the results of **Fig. 20a,** it can be seen that secondary-fracture conductivity will significantly influence the dimensionless pressure of the constant-rate well (W1); however, the dimensionless rate of the constant-BHP well (W2) is less affected. Furthermore, the time for W2 to exhibit a sharp rate decline is almost the same for different secondary-fracture conductivities. This suggests that secondary-fracture conductivity may not be a main factor causing rate loss of the constant-BHP well when it communicates with a constant-rate well. In addition, with a decrease of secondary-fracture conductivity, the interference will still be postponed, and the end of matrix linear flow is delayed. Fig. 20b illustrates the effect of the production rate of W1 on the flow behavior of the two-well system. The influence on the dimensionless pressure of W1 is throughout the well life, and gradually becomes negligible with production, caused by fluid feeding from the constant-BHP well (W2) after interference. With a decrease of production rate for W1, the duration of matrix linear flow is prolonged, and the rate of W2 undergoes a delayed rate loss. Therefore, for the two-well system containing a constant-rate well and constant-BHP well, altering operating conditions may be an effective treatment to reduce production damage. The results of Fig. 20c indicate that after the two wells are communicating, the effect of the number of sections on the behavior of two-well communication is not significant.

Conclusions

This paper presents a Laplace-domain hybrid model for analyzing the flow behavior associated with multiwell communication through secondary fractures in unconventional reservoirs. From the results of this investigation, the following important conclusions can be drawn:

- The new model developed in the Laplace domain can simulate multiwell communication through arbitrary fracture geometries and with variable fracture conductivity, without time discretization and with only grids for the fractures. The computations can be conducted at predetermined and discrete times with efficient performance. Further, flow behavior at very early time, such as fracture linear flow, can be captured accurately.
- Fluid flow between communicating wells, caused by pressure interference, significantly alters the flow signature compared with single (isolated) wells. Before interference, the communicating wells behave as single isolated wells and exhibit fracture-linear- and matrix-linear-flow periods. With a large contrast of secondary-fracture conductivity, number of connections, and operation conditions, the time to observed interference will be accelerated. Therefore, matrix linear-flow period may be masked, whereas fracture linear flow will always develop in any case. After interference, the flow behavior of the system will vary with operating conditions.
- For a two-well system with constant-rate operating conditions, when interference takes effect, the fluid sourcing will cause an upward trend for the transient response of the low-rate well and a downward trend for that of the high-rate well. The curves of the two wells will gradually converge to develop a short matrix-linear-flow period. With a delayed interference, the consequent matrix-linear-flow period may be absent. Production rate mainly influences fracture linear flow, and the effect on interference is not significant compared

with secondary-fracture conductivity. Although a larger number of connections will cause an earlier interference, the effect on the transient responses is not evident.

- For two communicating constant-BHP wells, the transient-response deviation will increase after interference. The primary fracture of the high-BHP well will source the low-BHP well throughout the production life. Hence, the high-BHP well will undergo rate loss, and even a negative rate. With high-conductivity secondary fractures, the production loss occurs very early. A larger contrast of BHPs for the two wells, and number of connections, will accelerate the rate loss.
- In a two-well communication system, when interference takes effect, the constant-BHP well is first sourced by the primary fracture of a constant-rate well. After a certain time, the constant-BHP well will exhibit a sharp rate decline. Operating conditions may be a main factor affecting rate loss of the constant-BHP well, instead of secondary-fracture conductivity, when it communicates with a constant-rate well. After the two wells are connected, the effect of the number of sections on the behavior of two-well communication is not significant.

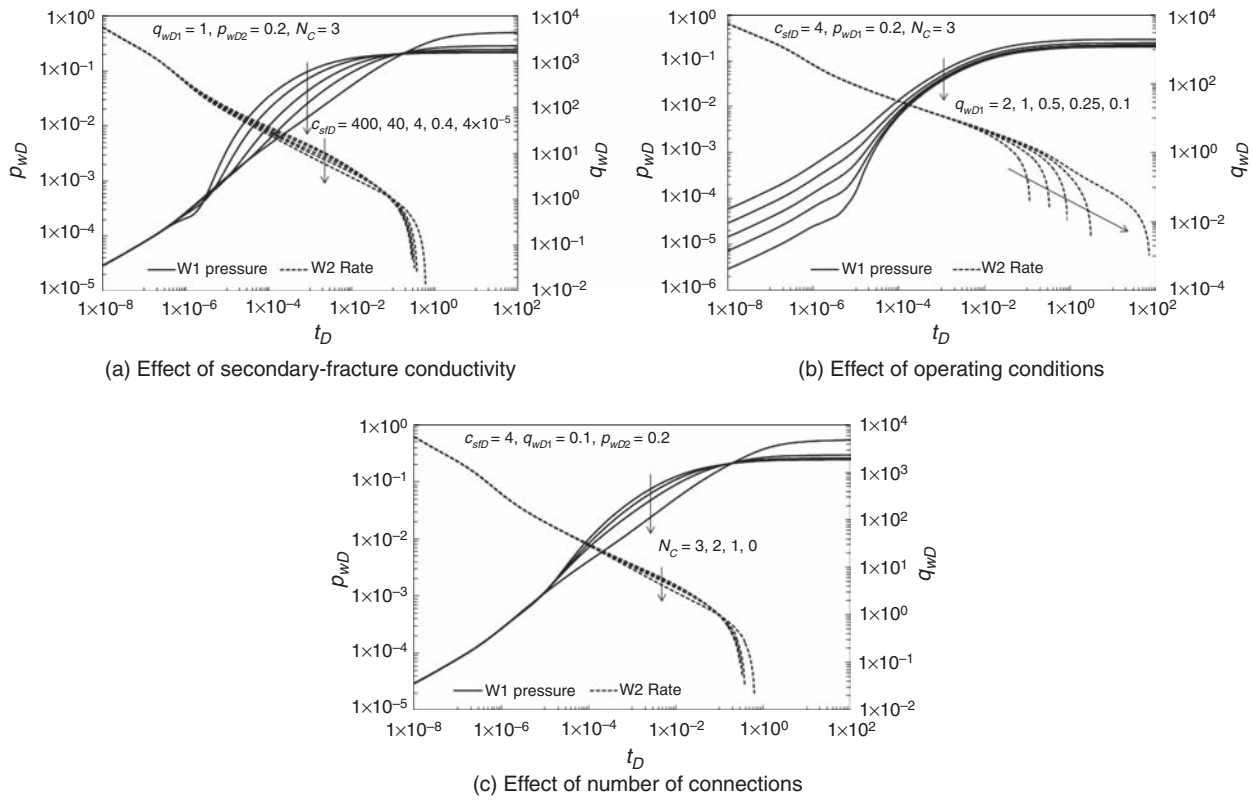

(a) Effect of secondary-fracture conductivity

(b) Effect of operating conditions

(c) Effect of number of connections

Fig. 20—Effect of key parameters on the transient responses of two communicating wells, one constant-rate well and one constant-BHP well.

Nomenclature

B = liquid formation volume factor, m^3/m^3
c_t = compressibility, Pa^{-1}
c_{lfD} = dimensionless fracture conductivity
C_D = dimensionless wellbore-storage coefficient
h = formation thickness, m
k_{lf} = fracture permeability, m
k_m = matrix permeability, m^2
N_{CP} = number of constant-BHP wells
N_{CR} = number of constant-rate wells
N_S = number of fracture segments
p = matrix pressure, Pa
p_i = initial pressure, Pa
p_{lf} = fracture pressure, Pa
p_{wI} = BHP of Ith constant-rate well, Pa
p_{wJ} = BHP of Jth constant-BHP well, Pa
q_{lf} = flow rate per unit fracture length from matrix under surface condition, m^2/s
q_{wI} = production rate of Ith constant-rate well, m^3/s
p_{wJ} = production rate of Jth constant-BHP well, m^3/s
q_r = reference flow rate, m^3/s
s_c = flow-chocking skin factor
t = time, seconds
$T_{Di,j}$ = dimensionless transmissibility between fracture segments i and j

$T^*_{Di,j}$ = dimensionless transmissibility between fracture segments i and j after the Star-Delta transformation
w_{lf} = fracture width, m
x = x-coordinate, m
x_i = x-coordinate of midpoint of fracture segment i, m
y = y-coordinate, m
y_i = y-coordinate of midpoint of fracture segment i, m
ΔL_i = length of fracture segment i, m
α_{Di} = coefficient of dimensionless pressure of fracture segment i
β_{Di} = coefficient of dimensionless flow rate of fracture segment i
γ_{Di} = dimensionless transmissibility between fracture segment i and the interface
ε = fracture direction, m
ζ = reference length, m
θ_i = inclination of fracture segment i, radians
μ = formation-fluid viscosity, Pa·s
ϕ_m = matrix porosity, fraction
ϕ_{lf} = fracture porosity, fraction
Ψ = set of the neighboring fracture segments of a certain segment

Superscripts and Subscripts

$-$ = Laplace transform
D = dimensionless
f = fracture
i = index of fracture segment
I = index of constant-rate well
J = index of constant-BHP well
l = primary fracture (p) or secondary fracture (s)
m = matrix
p = primary fracture
s = secondary fracture

Acknowledgments

We acknowledge that this study was partially funded by the National Program on Key Basic Research Project of China (973 Program) (No. 2015CB250902). We further would like to thank financial support of the National Natural Science Foundation of China (No. 51674273, No. 51574258, and No. 41672132). Clarkson and Qanbari would like to acknowledge the sponsors of Tight Oil Consortium for their support of this research. Clarkson would also like to thank Encana, Shell, and Alberta Innovates Technology Futures for their support of his Chair in Unconventional Gas and Light Oil Research (Department of Geoscience, University of Calgary).

References

Anderson, D. M. and Mattar, L. 2005. An Improved Pseudo-time for Gas Reservoirs With Significant Transient Flow. Paper presented at the Canadian International Petroleum Conference, Calgary, 1–3 August. PETSOC-2005-114. https://doi.org/10.2118/2005-114.

Awada, A., Santo, M., Lougheed, D. et al. 2016. Is That Interference? A Work Flow for Identifying and Analyzing Communication Through Hydraulic Fractures in a Multiwell Pad. *SPE J.* **21** (5): 1554–1566. SPE-178509-PA. https://doi.org/10.2118/178509-PA.

Cipolla, C. L., Warpinski, N. R., Mayerhofer, M. et al. 2010. The Relationship Between Fracture Complexity, Reservoir Properties, and Fracture-Treatment Design. *SPE Prod & Oper* **25** (4): 438–452. SPE-115769-PA. https://doi.org/10.2118/115769-PA.

Cipolla, C. L., Fitzpatrick, T., Williams, M. J. et al. 2011. Seismic-to-Simulation for Unconventional Reservoir Development. Paper presented at the Reservoir Characterization and Simulation Conference and Exhibition, Abu Dhabi, 9–11 October. SPE-146876-MS. https://doi.org/10.2118/146876-MS.

Clarkson, C. R., Nobakht, M., Kaviani, D. et al. 2012. Production Analysis of Tight-Gas and Shale-Gas Reservoirs Using the Dynamic-Slippage Concept. *SPE J.* **17** (1): 230–242. SPE-144317-PA. https://doi.org/10.2118/144317-PA.

Earlougher, R. C. and Ramey, H. J. 1973. Interference Analysis in Bounded System. *J Can Pet Technol* **12** (4): 33–45. PETSOC-73-04-04. https://doi.org/10.2118/73-04-04.

Gringarten, A. C. and Ramey, H. J. 1973. The Use of Source and Green's Functions in Solving Unsteady Flow Problems in Reservoirs. *SPE J.* **13** (5): 285–296. SPE-3818-PA. https://doi.org/10.2118/3818-PA.

Gupta, J. K., Zielonka, M. G., Albert, R. A. et al. 2012. Integrated Methodology for Optimizing Development of Unconventional Gas Resources. Paper presented at the SPE Hydraulic Fracturing Technology Conference, The Woodlands, Texas, USA, 6–8 February. SPE-152224-MS. https://doi.org/10.2118/152224-MS.

Habte, A. D. and Onur, M. 2014. Laplace-Transform Finite-Difference and Quasistationary Solution Method for Water-Injection/Falloff Tests. *SPE J.* **19** (3): 398–409. SPE-168221-PA. https://doi.org/10.2118/168221-PA.

Hazlett, R. D. and Babu, D. K. 2014. Discrete Wellbore and Fracture Productivity Modeling for Unconventional Wells and Unconventional Reservoirs. *SPE J.* **19** (1): 19–33. SPE-157379-PA. https://doi.org/10.2118/157379-PA.

Jia, P., Cheng, L., Huang, S. et al. 2015. Transient Behavior of Complex Fracture Networks. *J. Pet. Sci. Eng.* **132:** 1–17. https://doi.org/10.1016/j.petrol.2015.04.041.

Jia, P., Cheng, L., Huang, S. et al. 2016. A Semi-analytical Model for the Flow Behavior of Naturally Fractured Formations With Multi-Scale Fracture Networks. *J. Hydrol.* **537:** 208–220. https://doi.org/10.1016/j.jhydrol.2016.03.022.

Karimi-Fard, M., Durlofsky, L. J. and Aziz, K. 2003. An Efficient Discrete Fracture Model Applicable for General Purpose Reservoir Simulators. *SPE J.* **9** (2): 227–236. SPE-88812-PA. https://doi.org/10.2118/88812-PA.

King, P. R. 1989. The Use of Renormalization for Calculating Effective Permeability. *Trans Porous Med.* **4** (1): 37–58. https://doi.org/10.1007/BF00134741.

Lawal, H., Jackson, G., Abolo, N. et al. 2013. A Novel Approach to Modeling and Forecasting Frac Hits in Shale Gas Wells. Paper presented at the EAGE Annual Conference & Exhibition incorporating SPE Europec, London, 10–13 June. SPE-164898-MS. https://doi.org/10.2118/164898-MS.

Malpani, R., Sinha, S., Charry, L. et al. 2015. Improving Hydrocarbon Recovery of Horizontal Shale Wells Through Refracturing. Paper presented at the SPE/CSUR Unconventional Resources Conference, Calgary, 20–22 October. SPE-175920-MS. https://doi.org/10.2118/175920-MS.

Marongiu-Porcu, M., Lee, D., Shan, D. et al. 2016. Advanced Modeling of Interwell-Fracturing Interference: An Eagle Ford Shale-Oil Study. *SPE J.* **21** (5): 1567–1582. SPE-174902-PA. https://doi.org/10.2118/174902-PA.

Martinez, R. C., Rosinski, J., and Dreher, D. 2012. Horizontal Pressure Sink Mitigation Completion Design: A Case Study in the Haynesville Shale. Paper presented at the SPE Annual Technical Conference and Exhibition, San Antonio, Texas, USA, 8–10 October. SPE-159089-MS. https://doi.org/10.2118/159089-MS.

Moridis, G. J., McVay, D. A., Holditch, S. A. et al. 1994. The Laplace Transform Finite Difference (LTFD) Numerical Method for the Simulation of Compressible Liquid Flow in Reservoirs. *SPE Advanced Technology Series* **2** (2): 122–131. SPE-22888-PA. https://doi.org/10.2118/22888-PA.

Mukherjee, H. and Economides, M. J. 1991. A Parametric Comparison of Horizontal and Vertical Well Performance. *SPE Form Eval* **6** (2): 209–216. SPE-18303-PA. https://doi.org/10.2118/18303-PA.

Ozkan, E. and Raghavan, R. 1991. New Solutions for Well-Test-Analysis Problems: Part I—Analytical Consideration. *SPE Form Eval* **6** (3): 359–368. SPE-18615-PA. https://doi.org/10.2118/18615-PA.

Portis, D. H., Bello, H., Murray, M. et al. 2013. Searching for the Optimal Well Spacing in the Eagle Ford Shale: A Practical Tool-Kit. Paper presented at the Unconventional Resource Technology Conference, Denver, 12–14 August. SPE-168810-MS. https://doi.org/10.2118/168810-MS.

Qanbari, F. and Clarkson, C. R. 2012. Rate Transient Analysis of Stress-Sensitive Formations During Transient Linear Flow Period. Paper presented at the SPE Canadian Unconventional Resources Conference, Calgary, 30 October–1 November. SPE-162741-MS. https://doi.org/10.2118/162741-MS.

Sani, A. M., Podhoretz, S. B., and Chambers, B. D. 2015. The Use of Completion Diagnostics in Haynesville Shale Horizontal Wells to Monitor Fracture Propagation, Well Communication, and Production Impact. Paper presented at the SPE/CSUR Unconventional Resources Conference, Calgary, 20–22 October. SPE-175917-MS. https://doi.org/10.2118/175917-MS.

Sardinha, C., Petr, C., Lehmann, J. et al. 2014. Determining Interwell Connectivity and Reservoir Complexity Through Frac Pressure Hits and Production Interference Analysis. Paper presented at the SPE/CSUR Unconventional Resources Conference, Calgary, 30 September–2 October. SPE-171628-MS. https://doi.org/10.2118/171628-MS.

Stalgorova, E. and Mattar, L. 2013. Analytical Model for Unconventional Multifractured Composite Systems. *SPE Res Eval Eng* **16** (3): 246–256. SPE-162516-PA. https://doi.org/10.2118/162516-PA.

Stehfest, H. 1970. Numerical Inversion of Laplace Transforms. *Commun ACM* **13** (1): 47–49. https://doi.org/10.1145/361953.361969.

Van Everdingen, A. F. and Hurst, W. 1949. The Application of the Laplace Transformation Flow Problem in Reservoirs. *J Pet Technol* **1** (12): 305–324. SPE-949305-G. https://doi.org/10.2118/949305-G.

Yaich, E., Diaz de Souza, O. C., Foster, R. A. et al. 2014. A Methodology to Quantify the Impact of Well Interference and Optimize Well Spacing in the Marcellus Shale. Paper presented at the SPE/CSUR Unconventional Resources Conference, Calgary, 30 September–2 October. SPE-171578-MS. https://doi.org/10.2118/171578-MS.

Yu, W., Wu, K., Zuo, L. et al. 2016. Physical Models for Inter-Well Interference in Shale Reservoirs: Relative Impacts of Fracture Hits and Matrix Permeability. Paper presented at the Unconventional Resources Technology Conference, San Antonio, Texas, USA, 1–3 August. URTEC-2457663-MS. https://doi.org/10.15530/URTEC-2016-2457663-MS.

Zeng, F. and Zhao, G. 2010. The Optimal Hydraulic Fracture Geometry Under Non-Darcy Flow Effects. *J. Pet. Sci. Eng.* **72** (1): 143–157. https://doi.org/10.1016/j.petrol.2010.03.012.

Zhou, W., Banerjee, R., Poe, B. et al. 2014. Semi-Analytical Production Simulation of Complex Hydraulic Fracture Networks. *SPE J.* **19** (1): 6–18. SPE-157367-PA. https://doi.org/10.2118/157367-PA.

Appendix A: The Dimensionless-Variable Definitions

For the sake of simplicity, we introduce the following dimensionless variables.

The dimensionless pressure for matrix and fracture are defined, respectively, as

$$p_D = \frac{2\pi k_m h(p_i - p)}{q_r B \mu}, \quad \text{(A-1)}$$

$$p_{lfD} = \frac{2\pi k_m h(p_i - p_{lf})}{q_r B \mu}. \quad \text{(A-2)}$$

And the dimensionless BHP and production rate of well are given by

$$p_{wD} = \frac{2\pi k_m h(p_i - p_w)}{q_r B \mu}, \quad \text{(A-3)}$$

$$q_{wD} = \frac{q_w}{q_r}. \quad \text{(A-4)}$$

For dimensionless time,

$$t_D = \frac{k_m t}{\phi_m \mu c_{tm} \zeta^2}. \quad \text{(A-5)}$$

The dimensionless fracture flow rate q_{lfD} is defined as

$$q_{lfD} = \frac{2 q_{lf} \zeta}{q_r}. \quad \text{(A-6)}$$

In our model, we use the following definitions of dimensionless fracture conductivity and diffusivity, respectively:

$$c_{lfD} = \frac{k_{lf} w_{lf}}{k_m \zeta}, \quad \text{(A-7)}$$

$$\eta_{lfD} = \frac{k_{lf} \cdot \phi_m c_{tm}}{k_m \cdot \phi_{lf} c_{tlf}}. \quad \text{(A-8)}$$

Other dimensionless definitions are

$$x_D = \frac{x}{\zeta}, \quad \text{(A-9)}$$

$$y_D = \frac{y}{\zeta}, \quad \text{(A-10)}$$

$$\varepsilon_D = \frac{\varepsilon}{\zeta}, \quad \text{(A-11)}$$

$$x_{Di} = \frac{x_i}{\zeta}, \quad \text{(A-12)}$$

$$y_{Di} = \frac{y_i}{\zeta}, \quad \text{(A-13)}$$

$$\Delta L_{Di} = \frac{\Delta L_i}{\zeta}. \quad \text{(A-14)}$$

Appendix B: Derivation of the Linear System To Solve Transient Responses

The matrix-flow equation (Eq. 6b), the fracture-flow equation (Eq. 25), and the boundary condition (Eq. 27), which are combined to simulate the system, are listed as

$$\begin{cases} \boldsymbol{H} \cdot \overline{\boldsymbol{q}}_D - \boldsymbol{I} \cdot \overline{\boldsymbol{p}}_D = \boldsymbol{o} \\ \boldsymbol{B} \cdot \overline{\boldsymbol{q}}_{lfD} + \boldsymbol{T} \cdot \overline{\boldsymbol{p}}_{lfD} + \boldsymbol{R} \cdot \overline{\boldsymbol{p}}_{wD} = \boldsymbol{b} \\ \boldsymbol{R}^T \cdot \overline{\boldsymbol{p}}_{lfD} + \boldsymbol{L} \cdot \overline{\boldsymbol{p}}_{wD} = \boldsymbol{r} \end{cases}. \quad \text{(B-1)}$$

By the continuity of pressure and flow rate on the fracture surface (Eq. 28), we can rewrite Eq. B-1 as

$$\begin{cases} \boldsymbol{H} \cdot \overline{\boldsymbol{q}}_{lfD} - \boldsymbol{I} \cdot \overline{\boldsymbol{p}}_{lfD} = \boldsymbol{o} \\ \boldsymbol{B} \cdot \overline{\boldsymbol{q}}_{lfD} + \boldsymbol{T} \cdot \overline{\boldsymbol{p}}_{lfD} + \boldsymbol{R} \cdot \overline{\boldsymbol{p}}_{wD} = \boldsymbol{b} \\ \boldsymbol{R}^T \cdot \overline{\boldsymbol{p}}_{lfD} + \boldsymbol{L} \cdot \overline{\boldsymbol{p}}_{wD} = \boldsymbol{r} \end{cases}. \quad \text{(B-2)}$$

Further, Eq. B-2 can be rearranged as

$$\begin{cases} \boldsymbol{H} \cdot \overline{\boldsymbol{q}}_{lfD} - \boldsymbol{I} \cdot \overline{\boldsymbol{p}}_{lfD} + \boldsymbol{O} \cdot \overline{\boldsymbol{p}}_{wD} = \boldsymbol{o} \\ \boldsymbol{B} \cdot \overline{\boldsymbol{q}}_{lfD} + \boldsymbol{T} \cdot \overline{\boldsymbol{p}}_{lfD} + \boldsymbol{R} \cdot \overline{\boldsymbol{p}}_{wD} = \boldsymbol{b} \\ \boldsymbol{O}^T \cdot \overline{\boldsymbol{q}}_{lfD} + \boldsymbol{R}^{\mathrm{T}} \cdot \overline{\boldsymbol{p}}_{lfD} + \boldsymbol{L} \cdot \overline{\boldsymbol{p}}_{wD} = \boldsymbol{r} \end{cases}, \quad \text{(B-3)}$$

where, $\boldsymbol{O}$ is an $N_S \times N_{CR}$ zero matrix.

Finally, assembling the three subequations in Eq. B-3 to a matrix form, we can obtain the linear system to solve transient responses:

$$\begin{bmatrix} \boldsymbol{H} & -\boldsymbol{I} & \boldsymbol{O} \\ \boldsymbol{B} & \boldsymbol{T} & \boldsymbol{R} \\ \boldsymbol{O}^T & \boldsymbol{R}^T & \boldsymbol{L} \end{bmatrix} \cdot \begin{bmatrix} \overline{\boldsymbol{q}}_{lfD} \\ \overline{\boldsymbol{p}}_{lfD} \\ \overline{\boldsymbol{p}}_{wD} \end{bmatrix} = \begin{bmatrix} \boldsymbol{o} \\ \boldsymbol{b} \\ \boldsymbol{r} \end{bmatrix}. \quad \text{(B-4)}$$

SI Metric-Conversion Factors

cp × 1.0	E−03 = Pa·s
bbl × 1.589873	E−01 = m^3
ft × 3.048*	E−01 = m
md × 1.0	E+15 = m^2
psi × 6.894757	E+00 = kPa
psi^{-1} × 1.450377	E−01 = kPa^{-1}

* Conversion factor is exact.

Pin Jia is a PhD-degree candidate at China University of Petroleum, Beijing. He has studied at the college for 7 years. Jia's research interests include laboratory studies of the fundamental properties and flow behavior of naturally fractured reservoirs, transient-response analysis, and numerical modeling of fractured horizontal wells. He holds a BS degree in petroleum engineering from the China University of Petroleum, Beijing.

Linsong Cheng is a professor and director of the Department of Petroleum Engineering at the China University of Petroleum, Beijing. He has worked for 20 years at the college. Cheng's research interests include flow discipline of complex wells, flow dynamics of unconventional reservoirs, and the mechanism of heavy-oil development. He has authored or coauthored more than 80 technical papers and holds seven patents. Cheng holds a PhD degree from the China University of Petroleum, Beijing.

Christopher R. Clarkson is a professor and the AITF Shell/Encana Chair in Unconventional Gas and Light Oil Research in the Department of Geoscience and an adjunct professor with the Department of Chemical and Petroleum Engineering at the University of Calgary. His work focus in industry was on exploration for and development of unconventional gas (UG) and unconventional light oil (ULO) reservoirs. Clarkson's research focus since coming to the University of Calgary in 2009 has been on advanced reservoir-characterization methods for UG/ULO, such as rate- and pressure-transient analysis, flowback analysis, and core analysis. He is also interested in simulation of enhanced-recovery processes in UG/ULO, and how these processes can be used to reduce greenhouse-gas emissions. Clarkson leads an industry-sponsored consortium called "Tight Oil Consortium" (http://www.tightoilconsortium.com/), focused on the research topics for ULO reservoirs in western Canada. He holds a PhD degree in geological engineering from the University of British Columbia, Canada. The author of numerous articles in peer-reviewed scientific and engineering journals, Clarkson received the AIME Rossiter W. Raymond Memorial Award and the Alfred Noble Prize from the American Society of Civil Engineers for his paper "Application of a New Multicomponent Adsorption Model to Coal Gas Adsorption Systems" published in *SPE Journal* (September 2003). He was an SPE Distinguished Lecturer for the 2009–2010 lecture season.

Farhad Qanbari is a PhD-degree candidate in petroleum engineering at the University of Calgary. His research and work area interests include modeling and rate-transient analysis of oil and gas reservoirs, with focus on shale/tight oil and gas reservoirs. As a reservoir-engineering researcher in the Tight Oil Consortium at the University of Calgary, Qanbari has authored or coauthored numerous technical papers on rate-transient analysis of shale formations, and has analyzed production data from different shale oil and gas reservoirs in North America. He holds MSc and BSc degrees in petroleum reservoir engineering from Petroleum University of Technology, Iran, and an MEng degree in petroleum engineering from the University of Calgary.

Shijun Huang is an associate professor in the Department of Petroleum Engineering at the China University of Petroleum, Beijing. He has worked for 10 years at the college. Huang's research interests include fractured-reservoir description, heavy-oil development, and enhanced oil recovery of low-permeability reservoirs. He has authored or coauthored more than 40 technical papers. Huang holds a PhD degree from China University of Petroleum, Beijing.

Renyi Cao is an associate professor in the Department of Petroleum Engineering at China University of Petroleum, Beijing. He has worked for 11 years at the college. Cao's research interests include fractured-reservoir description, geology, and unconventional-reservoir development. He has authored or coauthored more than 35 technical papers. Cao holds a PhD degree from China University of Petroleum, Beijing.